High-temperature oxidation and hydrothermal corrosion of textured Cr$_2$AlC-based coatings on zirconium alloy fuel cladding

Chongchong Tang [*], Mirco Große, Sven Ulrich, Michael Klimenkov, Ute Jäntsch, Hans Jürgen Seifert, Michael Stüber [*], Martin Steinbrück

Institute for Applied Materials (IAM-AWP), Karlsruhe Institute of Technology (KIT), D-76021 Karlsruhe, Germany

ABSTRACT

Keywords:
Cr$_2$AlC MAX phase
Magnetron sputtering
Elemental multilayers
ATF
Oxidation
Hydrothermal corrosion

Alumina-forming MAX phase coatings reveal great potential for accident tolerant fuel (ATF) cladding applications due to their favorable physical and mechanical properties and excellent high-temperature oxidation resistance. The feasibility of Cr$_2$AlC MAX phase as protective coating on zirconium-alloy fuel claddings was explored focusing on high-temperature oxidation resistance in steam and hydrothermal corrosion performance in autoclave. Single-phase and basal-plane textured Cr$_2$AlC coatings (~6 μm thick) were synthesized on Zircaloy-4 substrate by thermal annealing of specifically designed, magnetron-sputtered Cr/C/Al elemental multilayers at 550 °C for 10 min. Additionally, a second Cr/Cr$_2$AlC bilayer coating design was fabricated aiming to eliminate potential rapid hydrothermal dissolution of Al during normal operating conditions. Micro-cracking appeared on both annealed coatings owing to thermal expansion differences between coating layer and substrate.

Growth of an adherent and dense α-Al$_2$O$_3$ scale during high-temperature oxidation in steam and of a thin passivating Cr$_2$O$_3$ layer during hydrothermal corrosion in an autoclave imply excellent combined oxidation and corrosion resistance of the textured Cr$_2$AlC coatings on Zircaloy-4. A self-healing capability via growth of alumina filling the micro-crack (annealing-induced) gaps was observed during high-temperature oxidation. However, partial delamination was seen for both coatings after short autoclave exposure and their mechanical properties (fracture toughness and adhesion strength) need further enhancement. Overall, tailored Cr$_2$AlC-based (multilayered) coatings can be attractive candidates as potential type of coated ATF claddings.

1. Introduction

Improving the efficiency, reliability, and safety in energy-related processes and technologies apparently demands advanced engineering structural materials (e.g. turbine blades and fuel claddings), specifically with excellent mechanical properties (strength and ductility) and high-temperature corrosion resistance, to withstand elevated temperatures and high stresses in various atmospheres [1]. Surface modification of high-strength engineering materials to enhance their corrosion/oxidation resistance enabling higher operating temperatures encompasses numerous techniques, including for examples thermal and environmental barrier coatings [2]. Zirconium-based alloys have been applied as fuel cladding in water-cooled nuclear reactors for several decades. They exhibit multiple desirable attributes, such as good hydrothermal corrosion resistance and irradiation stability during steady-state normal operation. However, rapid exothermic oxidation and severe mechanical degradation of zirconium alloy cladding tubes under design extension conditions threaten the reactor safety with the potential risk of hydrogen denotation, such as occurred during the Fukushima-Daiichi accidents [3,4]. Thus, enhancing the safety and reliability of water-cooled nuclear reactors via implementing advanced accident tolerant fuel (ATF) claddings has attracted great attention worldwide afterwards [5,6].

Surface modification of zirconium-based alloy cladding via deposition of oxidation-resistant coatings comprises one near-term evolutionary strategy of ATF claddings which preserves favorable neutronic and irradiation properties of state-of-the-art zirconium alloy cladding as substrate. Numerous coating design concepts have been proposed, including single-layer metallic or ceramic coatings, and multilayered coatings [7]. The thermodynamic stability under normal hydrothermal corrosion conditions and moderate oxide growth rate at elevated temperatures in oxidizing environments during accidental scenarios make chromia scale forming Cr-based or Cr-containing coating concepts

represent one most promising option [6,7]. Among these Cr-based coating materials, pure metallic Cr coatings have recently been intensively explored [8–17]. They offer advantages of easy fabrication, high thermal conductivity, good adhesion strength and irradiation resistance. However, the growth rate of Cr_2O_3 scale substantially accelerates once oxidizing temperatures exceed ~1200 °C [9,18]. The formation of volatile hydroxides in water vapor-containing atmosphere especially at high steam partial pressure and elevated temperatures can further restrict its protective capability [19]. Thus, it can be anticipated that a relatively thick Cr coating is needed to protect the zirconium alloy substrate from rapid oxidation and gain sufficient coping time during severe accidents. A thick metallic Cr layer could however cause abrupt degradation of the whole coated cladding system via rapid interdiffusion and formation of liquid phase at temperatures above the Cr—Zr eutectic point (1332 °C) [20,21].

Exploration and development of advanced robust Cr-containing compounds as coating materials for ATF applications, for instance alumina-forming materials instead of chromia-forming ones at elevated temperatures, enabling thin protective coating and higher failure temperature are of great interest. In comparison with Cr_2O_3 scale, Al_2O_3 scale possesses higher thermodynamic stability and lower growth rate in high-temperature oxidizing conditions [6]. Cr_2AlC, one of the most studied Al-containing MAX phases, appears to be promising as coating material for ATF application due to its high Cr content and exceptional high-temperature oxidation resistance via formation of an external and protective Al_2O_3 layer. $M_{n+1}AX_n$ (MAX) phases (M: transition metals, A: mainly group IIIA or IVA elements, X: C or N, n: typical 1–3) are layered ternary compounds which exhibit many attractive attributes combining properties characteristic of both ceramics and metals. Their combined property profiles are related to their layered crystal structures and special bonding characteristics [22,23]. For instance, Cr_2AlC is lightweight (5.24 g/cm^{-3}), elastically stiff (Young's modulus of 278 GPa, shear modulus of 116 GPa) and relatively soft (Vickers hardness of ~5 GPa) [24]. It also shows high electrical and thermal conductivity, good flexural and compression strengths, thermal shock resistance and intermediate fracture toughness [24,25]. Furthermore, selective oxidation of Al in some Al-containing MAX phases, particularly Ti_2AlC, Ti_3AlC_2 and the aforementioned Cr_2AlC, renders them excellent oxidation resistance and autonomous self-healing capacity (crack gap filled by growth of alumina scale and associated volume expansion) [26–29]. Hence, these Al-containing MAX phases have been proposed and evaluated as oxidation/corrosion protective coatings on Zr-based alloys [30–33] and other structural materials [34,35]. Moreover, the low thermal neutron absorption cross-section of these three elements warrant a negligible impact on the neutronic economy inside the reaction core for ATF application [36].

A range of methods, for instance physical vapor deposition (PVD) [23] and spraying techniques [37], have been implemented to synthesize MAX phase thin films and coatings. Synthesis of MAX phase materials via PVD (primarily by sputtering techniques) usually results in relatively thin and dense coatings. In case of PVD-synthesis of Ti-based MAX phases, high processing temperatures (typically >700 °C) are required which hinders their application on temperature-sensitive substrates [23]. In addition, Ti_2AlC coatings also display poor oxidation resistance at elevated temperatures in steam due to the formation of mixed oxide scales [38]. In contrast, Cr_2AlC coatings have been realized at relative low synthesis temperature at ~500 °C, via either intentional heating during deposition or exercising thermal annealing afterwards [39–41]. The low processing temperature makes it more favorable for depositing Cr_2AlC coating on fuel claddings than other MAX phase coatings since it will not significantly alter the structure and mechanical properties of the alloy substrate.

Recently, Zhang et al. found that Cr_2AlC coatings exhibit good chemical compatibility and mechanical integrity with Zircaloy substrate up to 800 °C [42]. At higher temperatures reaching 1000 °C, a diffusion barrier should be introduced to avoid fast inward diffusion of Al into the substrate. Thermal stability enhancement of Cr_2AlC coatings on Zr alloys by utilizing a double layer diffusion barrier (ZrN/AlN) was reported previously [43]. Our recent work demonstrated that magnetron sputtered Cr_2AlC coatings (and Ti_2AlC) act as a robust hydrogen diffusion barrier on Zircaloy-4 substrate, effectively suppressing hydrogen permeation into the substrate [44]. Ougier et al. reported that as-deposited Cr-Al-C and annealed Cr_2AlC coatings on Zr alloys are protective in dry and wet air at 1200 °C owing to the growth of a dense and adherent Al_2O_3-based scale [33]. Even though previous studies have demonstrated that PVD Cr_2AlC coatings on, for example superalloy [45] or titanium alloy substrates [46], possess excellent hot corrosion resistance and high-temperature oxidation resistance in air, but the hydrothermal corrosion behavior and high-temperature steam oxidation mechanism (prototypical to normal and accident conditions in nuclear reactor, respectively) of Cr_2AlC coatings on Zircaloy substrate have been rarely explored yet. In addition, the successfully synthesized Cr_2AlC coatings on Zircaloy substrate often are not single phase, but a mixture of binary compounds and MAX phase composite. The impure nature could hinder a clear understanding of the protective and potential degradation behavior of the coatings during service. Thus, it is necessary to synthesize phase-pure Cr_2AlC coating on Zircaloy substrate and examine its hydrothermal corrosion and steam oxidation performances to validate the feasibility for ATF application.

In the present work, we prepared single-phase and textured Cr_2AlC-based coatings on Zircaloy-4 substrates via thermal annealing of magnetron-sputtered nanoscale elemental multilayers. Two coating designs have been realized on Zircaloy-4 substrates, i.e. without or with a 1.5 μm thick Cr overlayer. The Cr overlayer aims to eliminate potential fast hydrothermal dissolution of Al during normal operation conditions [7]. Moreover, the specific basal-plane textured microstructure offers the potential to enhance oxidation/corrosion and irradiation resistance of the Cr_2AlC coatings [47,48]. High-temperature oxidation tests from 1000 °C to 1400 °C in steam and short-term autoclave tests have been conducted. Systematic characterizations have been carried out to evaluate their oxidation/corrosion mechanisms and kinetics, oxide scale microstructure and protective capability.

2. Experiment details

2.1. Coating deposition

The synthesis of the Cr_2AlC MAX phase coatings involves two steps, i. e. deposition of nanoscale Cr/C/Al multilayers via magnetron sputtering using three elemental targets and subsequent thermal annealing of the as-deposited multilayers in argon atmosphere. The thicknesses of the individual elemental layers of the multilayers were around 7 nm for chromium, 2 nm for carbon (graphite) and 4 nm for aluminum, calculated according to the stoichiometric ratio (i.e. 2:1:1) in Cr_2AlC and considering the theoretical densities of these three elements. Initially, Cr/C/Al multilayered stacks with around 3 μm thickness were deposited on the alumina substrates to investigate its crystallization behavior and identify the suitable annealing parameters for MAX phase formation. These experimental results have been published [41] and are not further discussed in this paper.

In this study, polished Zircaloy-4 sheets (10×10 or 10×15 mm^2) were used as substrates. The chemical composition (wt%) of the Zircaloy-4 is as follows: Sn~1.4, Cr~0.10, Fe~0.22, O~1000 ppm, Zr balance. The finished surface roughness (R_a) was ~50 nm. The as-deposited coatings consisted of two designs, which are schematically depicted in Fig. 1. A thin metallic layer acting as bonding layer have been frequently reported to improve the adherence of ceramic coatings onto metallic substrates [49]. Thus, both designs utilized a thin Cr interlayer (500 nm) aiming as bonding layer on the Zircaloy-4 substrate. In the first design (Type A), the periodical multilayered stacks have been repeated to ~640 stacks with a total thickness of ~6 μm. In the second design (Type B), the number of the periodical multilayered stacks were

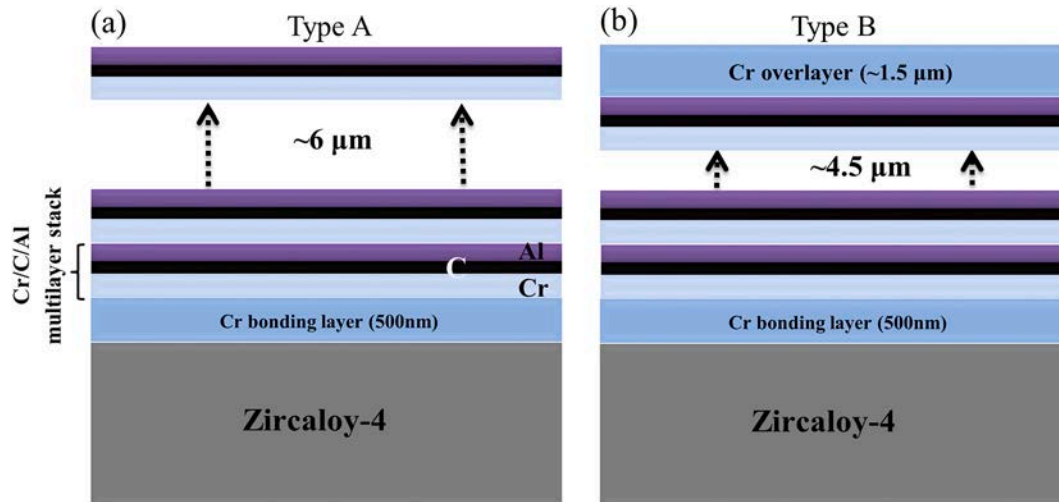**Fig. 1.** Schematic illustrations of the as-deposited coatings on Zircaloy-4 substrate. (a) Type A: without and (b) Type B: with a ~1.5 μm Cr overlayer. The blue, black and purple strips represent the Cr, C and Al nanolayer within the multilayer stacks, respectively.

reduced to 350, with a total thickness ~4.5 μm. Then, a ~1.5 μm Cr overlayer was deposited on top to avoid the potential rapid dissolution of Al within the coatings during reactor normal operations [7]. The thickness of the Cr overlayer was chosen to not considerably reduce the number of the multilayered stacks (i.e. Al reservoir for oxidation protection) and also to provide adequate hydrothermal corrosion resistance. Hence, the entire coating thickness was about 6.5 μm for both designs. Both sides of the samples were coated.

The deposition of the coatings was carried out using a laboratory PVD equipment, Leybold Z 550 coater. The substrates were ultrasonically washed in acetone for 10 min and then introduced into the vacuum chamber. They were placed on a rotating sample holder at a vertical distance of about 7 cm from the sputtering target inside the chamber. The chamber was evacuated to a base pressure of about 1×10^{-4} Pa and the substrate was plasma-etched for 10 min in a pure Ar atmosphere (grade 6 N) with a gas pressure of 0.5 Pa and a radio frequency (RF) power of 500 W. The power was fixed at 200 W for the three elemental targets during deposition, with RF power supplied on the chromium and aluminum targets and direct current (DC) power supplied on the graphite target. The argon working pressure was 0.5 Pa, and the substrates were grounded and not intentionally heated during deposition. Their deposition rates were measured in same setup previously and were approximately 0.8 nm/s for Cr, 0.2 nm/s for C and 1.1 nm/s for Al. The sputtering device operates in a stop-and-go mode through an individual steering of samples and shutter movement to realize the multilayered design. The sample holder and shutter rotated from one target position to another one, and different dwell times were pre-defined at each individual target position. The Cr interlayer and overlayer were deposited by only switching on the Cr target power without rotating the substrate holder. More detailed information on the deposition of the nanoscale elemental multilayers are given in references [38,41].

2.2. Annealing, oxidation and autoclave tests

The as-deposited coatings were annealed in pure Ar (grade 6 N) at atmospheric pressure using a commercial thermal balance (NETZSCH STA-449 F3 Jupiter) to promote the growth of Cr_2AlC MAX phase via diffusion-controlled solid-state reaction from the Cr/C/Al multilayered stacks. Based on our previous findings for thermally induced Cr_2AlC MAX phase formation on alumina substrates, the suitable annealing parameters are 550 °C and 10 min in argon atmosphere [41,44]. The heating and cooling rates were fixed at 10 K/min. The experimental results (next section) will confirm that the Cr bonding layer and overlayer remain intact without manifest reaction or diffusion to the

multilayered stacks under such annealing conditions. In addition, the relatively low annealing temperature and short dwell time herein are favorable for application on fuel claddings which will not significantly modify the microstructure and mechanical properties of the Zircaloy-4 substrate. After annealing in argon, the coated samples were then subjected to steam oxidation and autoclave tests.

Isothermal oxidation and transient oxidation tests in steam atmosphere were conducted to examine the oxidation performance of both uncoated and coated Zircaloy-4 samples. The size of the sample herein is $10 \times 10 \times 0.575$ mm^3. Isothermal tests at 1000 °C and transient tests from 300 °C to 1200 °C were carried out also using the NETZSCH thermal balance with a water vapor furnace. The mass change of the samples during the oxidation testing was recorded in-situ. The steam flow rate was 3 g/h produced by a steam generator. The steam was injected directly into the reaction tube from the top enabling a nearly pure steam atmosphere at the sample position. Transient oxidation tests from 500 °C to 1400 °C were conducted using a horizontal alumina tube furnace, the so-called BOX rig with higher temperature capability up to 1700 °C [50]. During the steam oxidation phase, the atmosphere consisted of 20 l/h Ar and 20 g/h H_2O (resulting in ~55 vol% H_2O). A quadrupole mass spectrometer (Balzers GAM 300) was installed and connected to the off-gas to measure its composition, especially hydrogen to quantitatively determine the oxidation kinetics. The heating rates in the ramp period were 10 K/min.

Short-term autoclave tests of both uncoated and coated Zircaloy-4 samples were conducted to assess the hydrothermal corrosion performance of the coatings. For that purpose, the samples are $15 \times 10 \times 0.60$ mm^3 within a 2 mm diameter suspension hole. In the case of first design (i.e. Type A without Cr overlayer), one side of the substrates was not covered with the Cr bonding layer. The autoclave tests were carried out in a static autoclave (Westinghouse test T949) with 360 °C pure water and 18.8 MPa pressure (PWR normal operation). The test duration was 3 days.

2.3. Characterization

The phase composition and constitution of the coatings, including as-deposited, annealed and oxidized coatings, were analyzed by X-Ray diffraction (XRD, Seifert PAD II diffractometer) with Cu Kα1 radiation (λ 0.15406 nm, 40 kV and 30 mA). A classical Bragg–Brentano geometry (θ-2θ) was applied with a step size of 0.002° and a scan speed at 1°/min. The potential preferred orientation of specific phases was analyzed by comparing with standard JCPDS/ICDD cards. Before and after testing, the mass of the specimens was measured using an analytical balance.

The morphology and chemical composition of both surfaces and cross-sections of the uncoated and coated Zircaloy-4 samples were examined by a field-emission scanning electron microscopy (SEM, Philips XL30S). The specimens were embedded in epoxy resin, then polished using SiC paper and diamond suspensions for cross section investigations. The SEM facility is equipped with an energy dispersive X-Ray spectrometer (EDS) for element analysis.

Selected annealed and oxidized samples were also evaluated by high-resolution transmission electron microscopy (HRTEM, FEI Tecnai 20 FEG). The cross-sectional lamellas for HRTEM analyses were prepared by focused ion beam (FIB) in situ lift-out technique (Auriga™, Carl Zeiss). The characterizations were focused on identification of the phase formation, grain size and orientation, and interfacial microstructure at various positions across the samples using different imaging modes, including bright and dark field, scanning-TEM, and high-angle annular dark-field imaging (HAADF).

3. Results

3.1. Phase formation and microstructure

The XRD patterns of as-deposited and 550 °C annealed coated Zircaloy-4 samples are presented in Fig. 2. All XRD signals marked by Zr (JCPDS #05-0665) are attributed to the Zircaloy-4 substrate. The Al (111) (JCPDS #04-0787) and Cr (110) (JCPDS #06-0694) reflections were identified for as-deposited coatings of Type A (without Cr overlayer). A weak diffraction intensity of the Al (111) peak was seen because of the low thickness and nanocrystallinity of the Al layers. The broad feature and small shift towards lower angle of the Cr (110) signal can be attributed to its nanocrystallization and abundant growth defects during deposition. As expected consequence of the nanoscale design of the as-deposited multilayers, the multilayered stacks are suggested to be composed of nanocrystalline Cr and Al layers as well as amorphous carbon layers. The Al (111) signal was barely detected for the as-deposited coatings of Type B because of the presence of the Cr overlayer. Further, the Type B coatings with the Cr overlayer showed an additional broad diffraction signal which is centered around the Cr (200) reflection and superimpose a substrate signal there. This suggests that the nanoscale multilayered arrangement restricts the growth of the chromium nanolayers with specific preferential orientation, i.e. Cr (110), the most densely packed plane [41]. The thick Cr overlayer, on the other hand, can grow randomly without particularly preferential orientation.
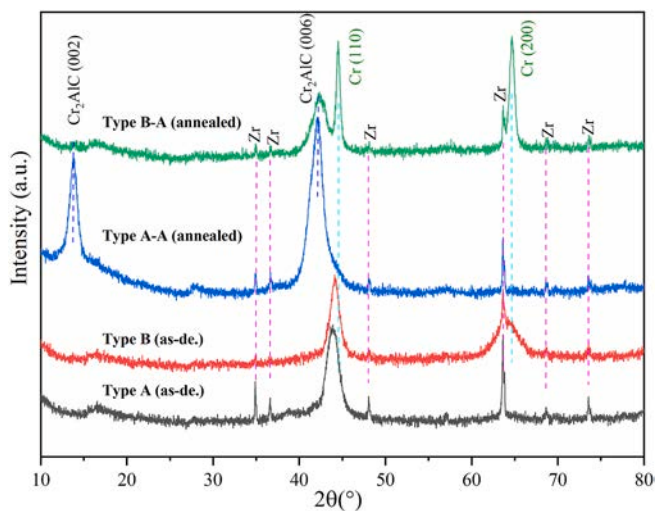

Fig. 2. XRD patterns of as-deposited and annealed coatings on Zircaloy-4 substrates. The Type A-A and Type B-A represent the two designs of coatings after annealing at 550 °C and 10 min in argon.

After annealing, the Type A-A coatings (annealed, without Cr overlayer) only exhibited diffraction signals belonging to the Cr_2AlC MAX phase (JCPDS #29-0017), i.e. Cr_2AlC (002) and (006) planes. No other impurity phases, such as binary carbides or intermetallic compounds, were recognized. Thus, the Cr/C/Al elemental multilayered stacks have transformed to the Cr_2AlC MAX phase via thermally induced solid-state diffusion reaction. The high intensity and exclusive {00l} diffraction reflections detected by XRD indicate that the Cr_2AlC coating possesses a basal-plane textured structure, in consistence with our previous findings [41]. In addition, both diffraction peaks are quite broad, showing nanocrystalline feature of the Cr_2AlC layer. For the Type B-A coatings (annealed, with Cr overlayer), only Cr_2AlC and Cr phases are observed after annealing. Absence of other phases related to the coatings reveals that no apparent reaction occurs between the Cr overlayer and the Cr/C/Al multilayered stacks during annealing. While, the signal associated with the Cr_2AlC (002) plane was barely detected, likely owing to its relatively lower intensity and limited probing depth of the X-ray. The diffraction peaks attributed to Cr became significantly sharper and were slightly shifted to higher diffraction angles compared to those before annealing, which indicates grain coarsening effect, recovery of growth defects and reduction of residual stresses (intrinsic and thermal stresses) within the Cr overlayer after thermal annealing [51].

The surface and cross-sectional morphologies inspected by SEM of the coated Zircaloy-4 samples before and after 550 °C annealing are shown in Figs. 3 and 4, respectively. Both as-deposited coatings are dense, smooth and free of macroscale defects, as depicted in Fig. 3(a) and (c). Even though both coatings remained adherent and uniform without spallation, parallel micro-cracks (longitudinal/channel cracks) were observed (highlighted in Fig. 3(b) and (d) via dashed lines) on the surfaces after annealing. As displayed in Fig. 4 for both designs of coatings after annealing, the Cr layer (both bonding layer and overlayer) and the Cr_2AlC layer inside the two types of coatings could be easily distinguished via their different contrasts; their interfaces are sharp and clear. The overall coating thicknesses including each individual sublayer are consistent with the predicted values based on measured deposition rates, as indicated in Fig. 4. These features manifest that no obvious interaction and/or interdiffusion between the relatively thick Cr layer (bonding layer and overlayer) and the MAX phase formation Cr/C/Al multilayer during the annealing stage.

The annealed coatings were additionally characterized by TEM to clarify the phase formation and interfacial microstructure. Fig. 5 shows an overview bright-field TEM image and HRTEM images at two interfaces and inside the Cr_2AlC layer. Fig. 6 displays the EDS mapping of Cr and Al at the Cr/Cr_2AlC interface. As shown in Fig. 5, the underneath Zircaloy-4 substrate consists of randomly-orientated, coarse grains. A compact microstructure without macro-size growth defects is evidenced for the coatings. A columnar structure along the growth direction of the Cr bonding layer is evident from the cross-sectional overview TEM image at low magnification. The Cr_2AlC layer is free of columnar grain boundaries and composed of nano-crystallites. Annealing of the multilayered stacks, as proved previously [41], resulted in platelet-like, elongated grains of the final MAX phase coatings. The HRTEM image (number 1) revealed that a thin interdiffusion/reaction layer, around 10 nm thick, established at the Zircaloy-4 substrate/Cr bonding layer interface after annealing, as indicated by the black arrows. No apparent interdiffusion layer was found at the Cr/Cr_2AlC interface (number 2). In addition, the EDS mapping results in Fig. 6 demonstrate no obvious chemical gradient of Cr and Al across the Cr/Cr_2AlC interface.

Transformation of the nanoscale elemental multilayers to the Cr_2AlC MAX phase is unquestionably proved by the unique layered structure and the inserted FFT image, Fig. 5 (number 3). However, the image disclose a relatively low degree of crystallinity and the grain size is only approximately 10 nm of the Cr_2AlC layer. The low annealing temperature combined with the short dwell time here, i.e. 550 °C 10 min, logically limited the growth and coalescence of the crystallites.
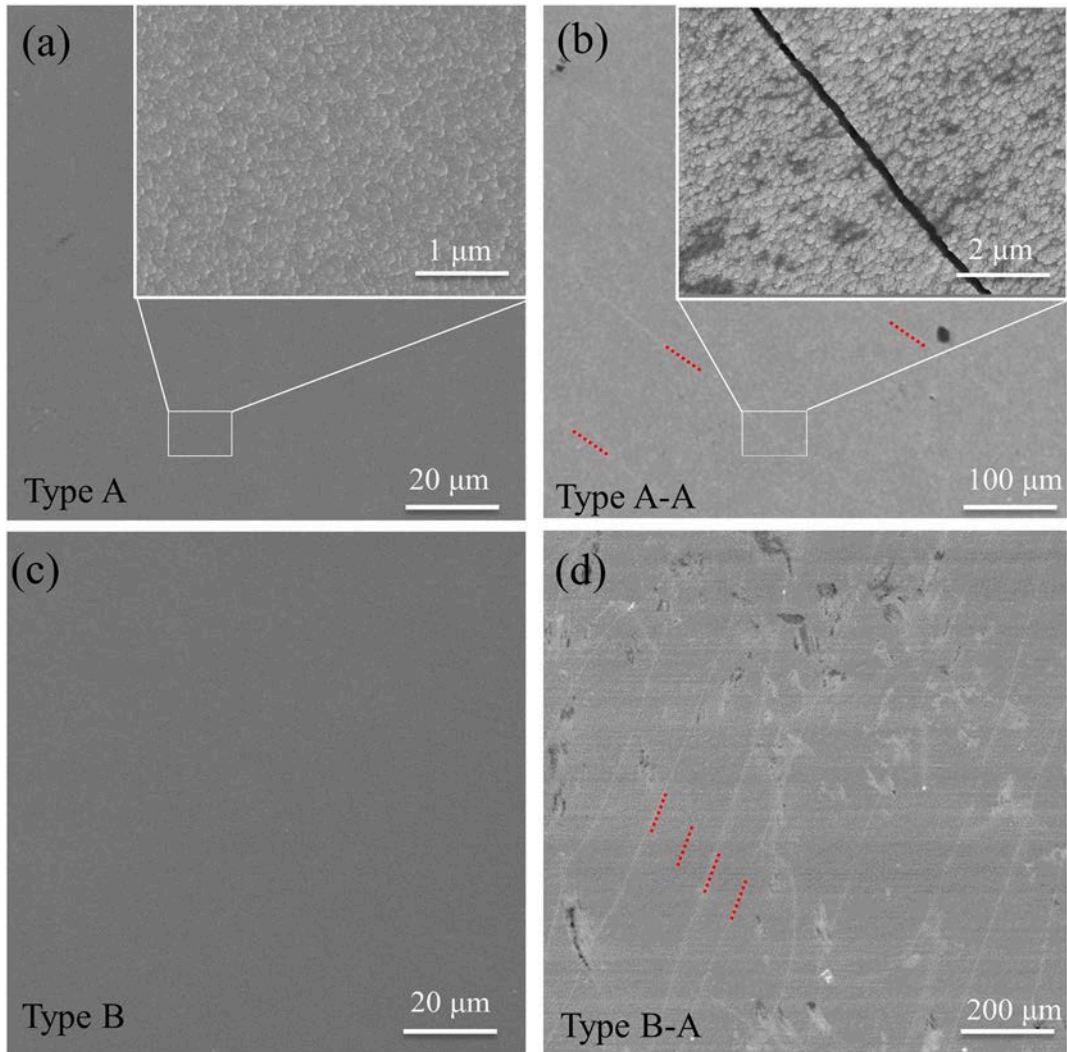
Fig. 3. Surface morphologies of the as-deposited and annealed coatings on Zircaloy-4 substrates. (a) Type A and (b) Type A-A, inserts are high-magnification images; (c) Type B and (d) Type B-A.
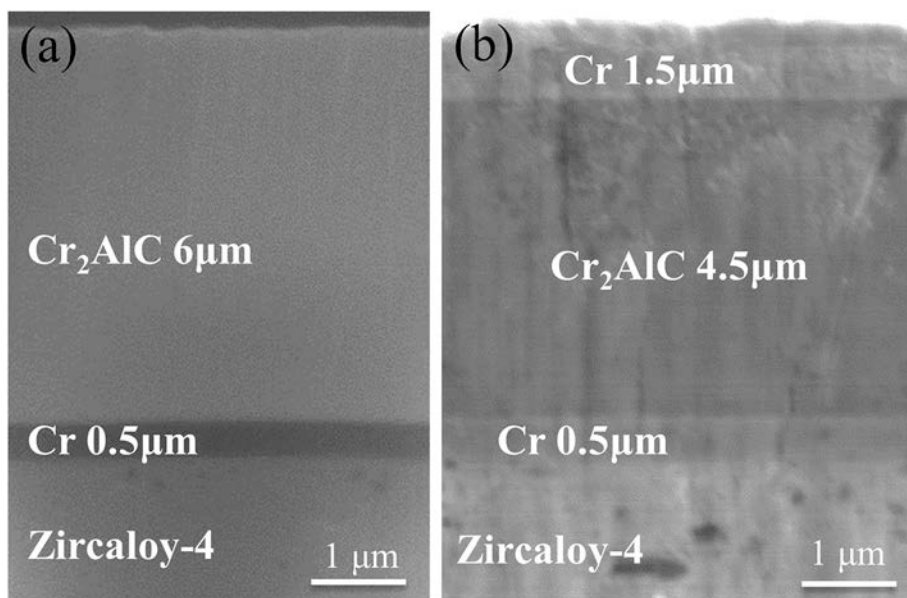

Fig. 4. Cross-sectional morphologies of the annealed coatings on Zircaloy-4 substrates. (a) Type A-A, (b) Type B-A.
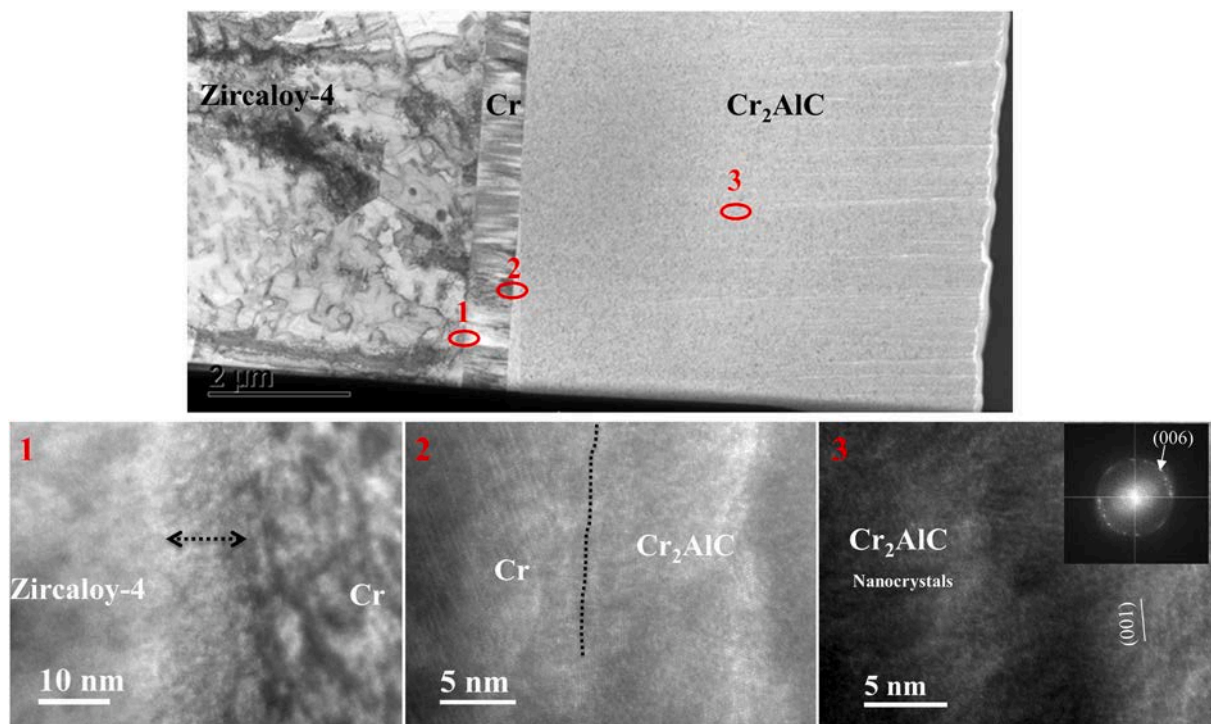
Fig. 5. TEM images of the Type A-A (without Cr overlayer) coated Zircaloy-4. The upper image is a general view and the images below are detailed views at two interfaces and in the middle of the Cr_2AlC layer as marked by different numbers. The inset in image number 3 describes the corresponding FFT of the image.
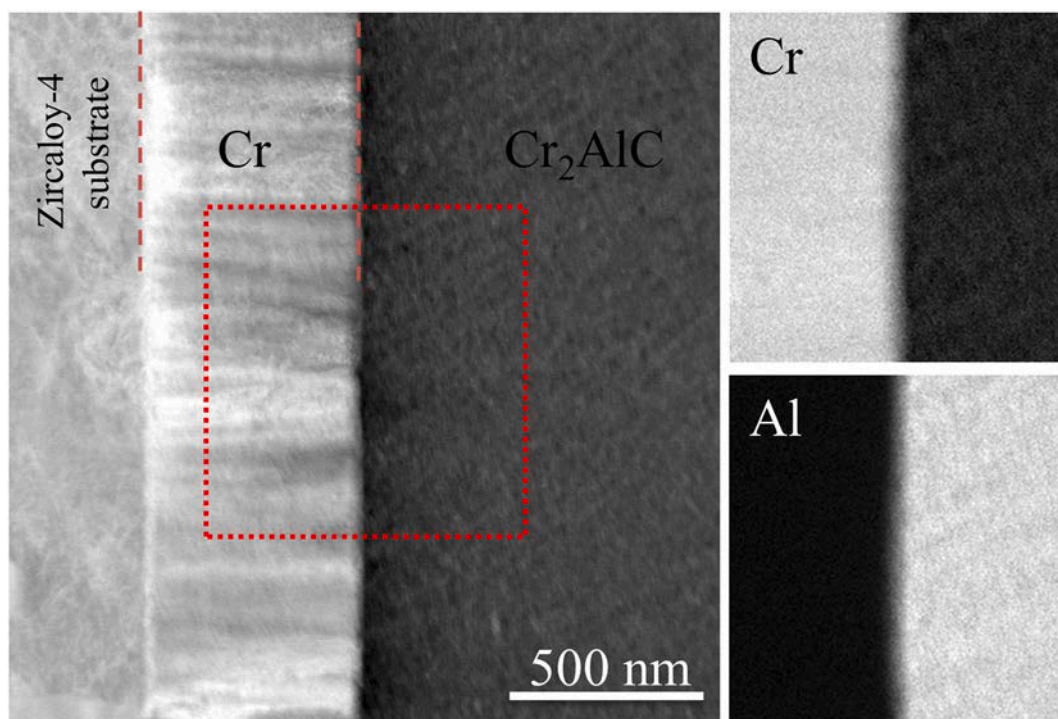

Fig. 6. EDS mapping of Cr and Al at the Cr/Cr_2AlC interface of the Type A-A (without Cr overlayer) coated Zircaloy-4.

3.2. High-temperature oxidation in steam

3.2.1. Isothermal tests

Fig. 7 shows the oxidation rate, i.e. mass gain per unit area as a function of oxidation time, of one uncoated reference and two coated Zircaloy-4 samples at 1000 °C in steam for 1 h. The inserted images exhibit the post-test surface appearances of the coated samples. The oxidation kinetics of uncoated Zircaloy-4 obeyed roughly a parabolic law, as indicated by the fitting curve and related coefficients. Its mass gain reached 25.1 mg/cm^2 after oxidation exposure. The high-temperature oxidation resistance of the two coated Zircaloy-4 was significantly improved compared to the uncoated Zircaloy-4. But their
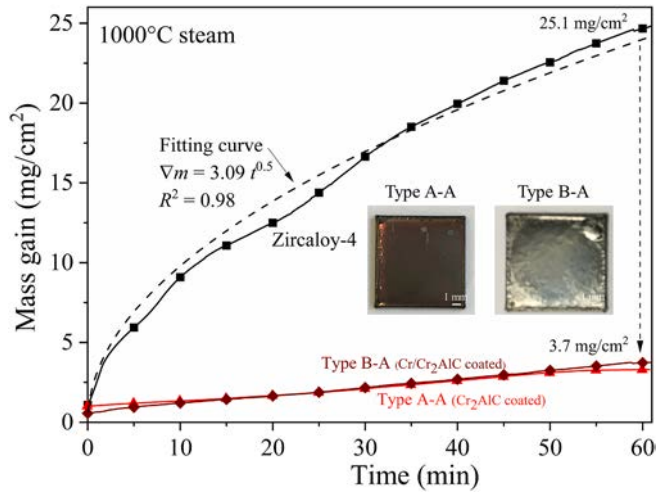
Fig. 7. Oxidation rate of the uncoated and two coated Zircaloy-4 samples at 1000 °C in steam for 1 h. The inserted images show the post-test surface appearances of the coated samples. The dashed line shows the fitting result with parabolic law for uncoated Zircaloy-4. Here, the Cr_2AlC and Cr/Cr_2AlC represent the coatings without and with the Cr overlayer after annealing, respectively.

oxidation rates are difficult to fit into a typical power law owing to small mass gains and oxidation contributions from uncoated regions. Their weight gains were similar, around 3.7 mg/cm², which means these coated samples showed a reduction of weight gain by a factor of roughly 7 times and only 14.7% of the weight gain of the uncoated Zircaloy-4.

The inserted images reveal that both coatings were adherent after oxidation, showing no spallation but displaying different colors (owing to the growth of different oxide scales on the surface, i.e. Al_2O_3 on Type A-A and Cr_2O_3 on Type B-A, which will be shown later). Severe oxidation of the Zircaloy-4 substrate occurred adjacent to the improper coated

or uncoated edges/corners (i.e. edge effect, confirmed later via cross-section examination). Overall, the two coated samples exhibited extremely slow oxidation rates without accelerated oxidation or breakaway oxidation phenomenon throughout the exposure.

The surface and cross-sectional morphologies of the uncoated and two coated Zircaloy-4 samples after oxidation are presented in Fig. 8. As shown in Fig. 8(a) and (b), the oxide scales on both coatings are relatively smooth and free of large nodules. The oxide scale was mainly composed of fine oxide crystals for the Type A-A coating (Cr_2AlC), while needle-like and equiaxed oxide grains grew on the surface of the Type B-A coating (Cr/Cr_2AlC). As identified and confirmed by cross-sectional SEM and XRD analyses of the oxidized samples (please see Figs. 8 and 9), the outermost layer of the oxide scales are α-Al_2O_3 and Cr_2O_3, respectively. Thus, oxidation of the two types of coatings resulted in growth of α-Al_2O_3 scale for Cr_2AlC and Cr_2O_3 scale for Cr/Cr_2AlC on the surface. The α-Al_2O_3 scale, Fig. 8(a), revealed a substantially denser surface microstructure compared to that of the Cr_2O_3 scale, Fig. 8(b), which consisted of fine voids. The cross-sectional SEM image in Fig. 8(c) confirms that a thin and dense α-Al_2O_3 scale grew on the Cr_2AlC coating, which acts as an effective diffusion barrier and inhibits oxidation of the substrate for at least 1 h exposure in steam at 1000 °C. The thickness of the α-Al_2O_3 scale is roughly 0.6 μm and the calculated mass gain based on this scale thickness is ~0.12 mg/cm².

Oxidation of the Cr/Cr_2AlC coating resulted in the formation of a more complex, multilayered configuration of structure, consisting of several sublayers. The sequence of the sublayers from surface to interior region follows $Cr_2O_3/Cr/Al_2O_3$/un-oxidized coating, Fig. 8(d). Nearly 80% of the Cr overlayer was oxidized, and the growth rate of the Cr_2O_3 scale was obviously much faster than that of α-Al_2O_3 scale. Steam penetrated the Cr_2O_3 scale and the residual Cr layer to oxidize the Cr_2AlC coating beneath, forming a thin α-Al_2O_3 scale at the Cr/Cr_2AlC interface. The absence of XRD signals from the alumina, binary chromium carbides and un-oxidized Cr_2AlC phases for Cr/Cr_2AlC coating in Fig. 9 is due to the relatively thick Cr_2O_3 + Cr surface layer and limited probing depth of the X-ray. The relatively porous microstructure of the
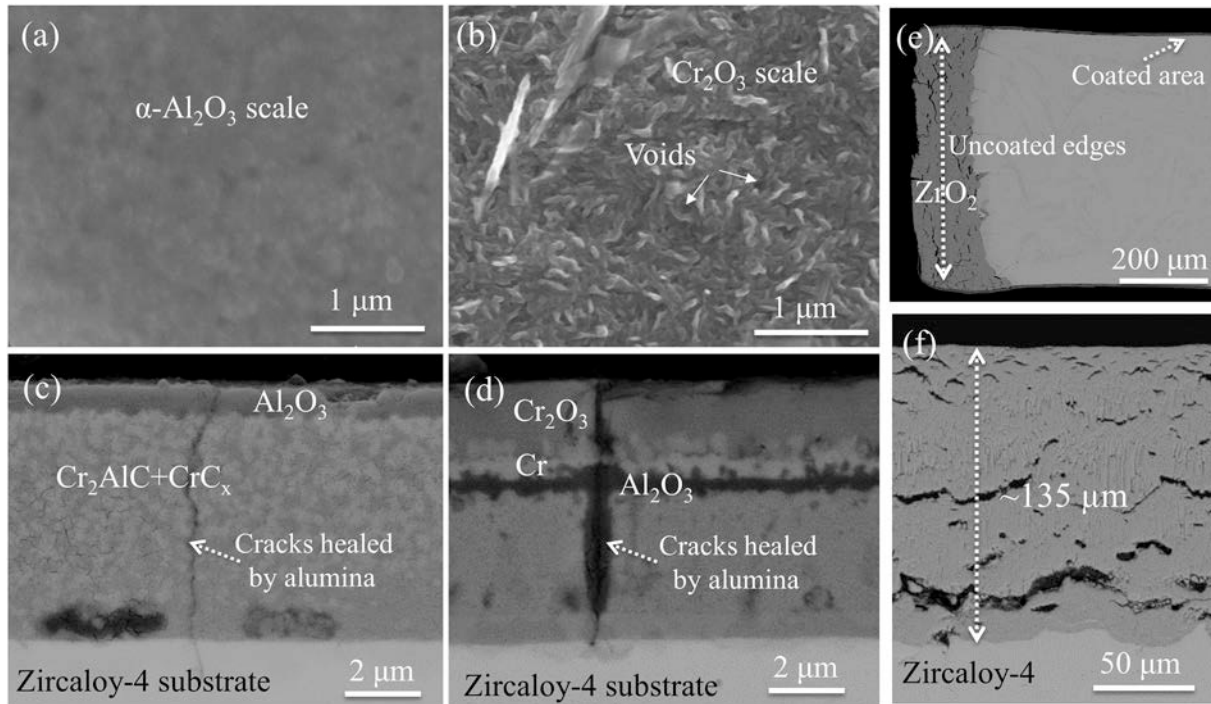

Fig. 8. Surface and cross-sectional morphologies of the uncoated and two coated Zircaloy-4 samples after oxidation at 1000 °C in steam for 1 h. Surface views: (a) Type A-A (Cr_2AlC) and (b) Type B-A (Cr/Cr_2AlC) coated Zircaloy-4 samples. Cross-sectional views: (c) Type A-A (Cr_2AlC) and (d), (e) Type B-A (Cr/Cr_2AlC) coated Zircaloy-4 samples, (f) uncoated Zircaloy-4. Figures c, d, e and f are taken in back-scattered electrons (BSE) mode.
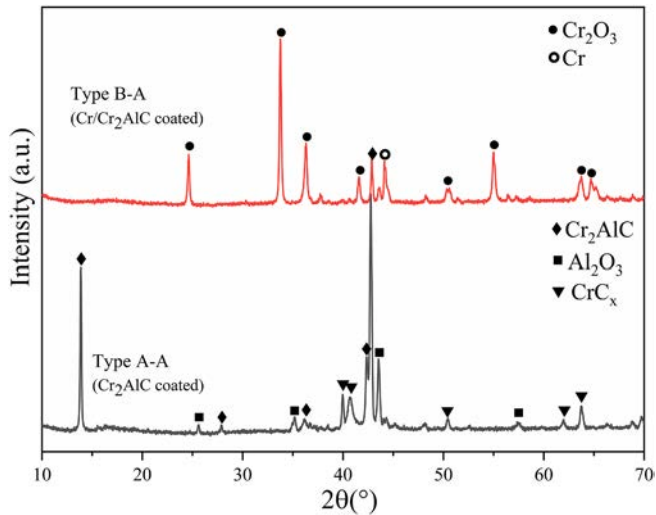
Fig. 9. XRD patterns of two coated Zircaloy-4 samples after oxidation at 1000 °C in steam for 1 h.

Cr_2O_3 scale (Fig. 8(b)) in conjunction with columnar grain boundaries within the Cr overlayer can act as short-circuit diffusion paths for steam, leading to the internal oxidation of the Cr_2AlC layer. The calculated mass gain here was several times higher compared to the Cr_2AlC coating, ~0.45 mg/cm^2.

Even though micro-cracks existed before oxidation, no noticeable oxidation of the substrate beneath the cracks and a self-healing capability via growth of alumina filling the crack gap were seen for both coatings. As shown in Fig. 8(c), (d) and (e), the micro-cracks were completely healed after oxidation at 1000 °C for 1 h. The dense alumina scale acted as an effective diffusion barrier and suppressed further oxidation of regions adjacent to the cracks. Two contrasts of white and gray domains within the Cr_2AlC layer, especially in Fig. 8(c) for the Cr_2AlC coating, could be distinguished. The domain with brighter color was deficient in Al and enriched in Cr and C, presumably to be the CrC_x

(Cr_7C_3 and/or Cr_3C_2 phases) as indicated in the XRD patterns (Fig. 9) [26,33]. The other more gray phase represents original Cr_2AlC grains. In addition, some voids were observed at the coating/substrate interface, as displayed in Fig. 8(c), and the Cr bonding layer could hardly be distinguished now. The explanations arise from the Kirkendall effect [52] via interdiffusion between the Cr bonding layer and the Cr_2AlC layer as well as between the coating (especially Al, see below EDS mapping results) and the substrate. The low-magnification image of Fig. 8(e) confirms the edge effect for the coated samples during oxidation, which shows thick ZrO_2 layer growth on the uncoated edges. In the coated surfaces, the coatings are protective and adherent.

In comparison, oxidation of uncoated Zircaloy-4 under the same condition led to the growth of a porous, less-protective ZrO_2 layer with substantial pores and cracks, Fig. 8(e). The thickness of the ZrO_2 layer was about 135 μm, more than 200 times thicker than the oxide scales formed on the coatings. The microstructure and thickness of the oxide layer is in accordance with earlier findings [53].

To confirm the multilayered configuration and mutual diffusion behavior within the coatings during oxidation, an EDS elemental mapping result of the Cr/Cr_2AlC coating after oxidation is shown in Fig. 10. From the surface to the interior zone, a multilayered structure following the sequence of $Cr_2O_3/Cr/Al_2O_3/Cr_2AlC + CrC_x$ was derived by EDS mapping, as previously seen in Fig. 8(d). The principal diffusion element identified is Al and the spatial distribution of aluminum in the Cr_2AlC layer became uneven after oxidation. Rapid local diffusion of Al from the Cr_2AlC layer into the Cr bonding layer and beneath Zircaloy-4 substrate was shown, most probably after the columnar grain boundaries of the Cr bonding layer. There was negligible mutual diffusion between the Cr bonding layer and the Zircaloy-4 substrate.

3.2.2. Transient tests

The mass gain curves and oxide scale structures obtained in transient tests from 300 °C to 1200 °C in steam are presented in Fig. 11. Noticeably, oxidation rate of the uncoated Zircaloy-4 was considerably faster than that of the coated ones. Furthermore, oxidation rate of the uncoated Zircaloy-4 accelerated from approximately 900 °C associated with increased mass gain rate. Both coated samples had comparable
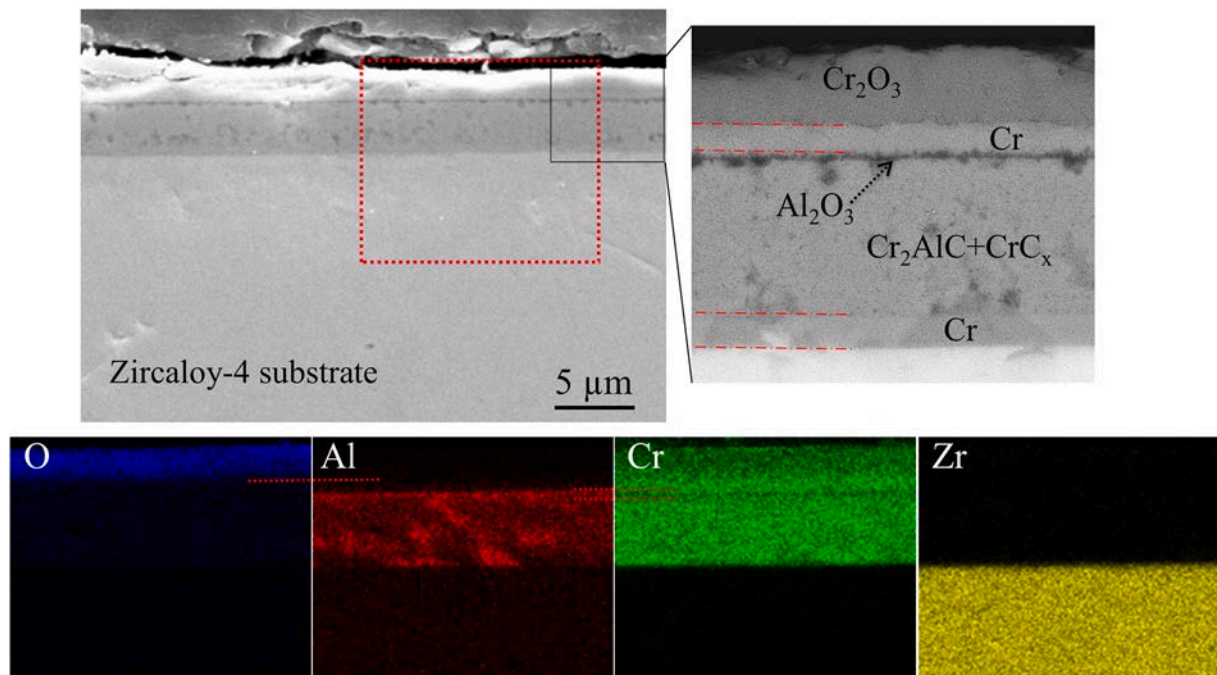

Fig. 10. Cross-sectional SEM image of the Type B-A (Cr/Cr_2AlC) coated Zircaloy-4 and corresponding EDS elemental mapping in the area marked by the red rectangle after oxidation at 1000 °C in steam for 1 h.
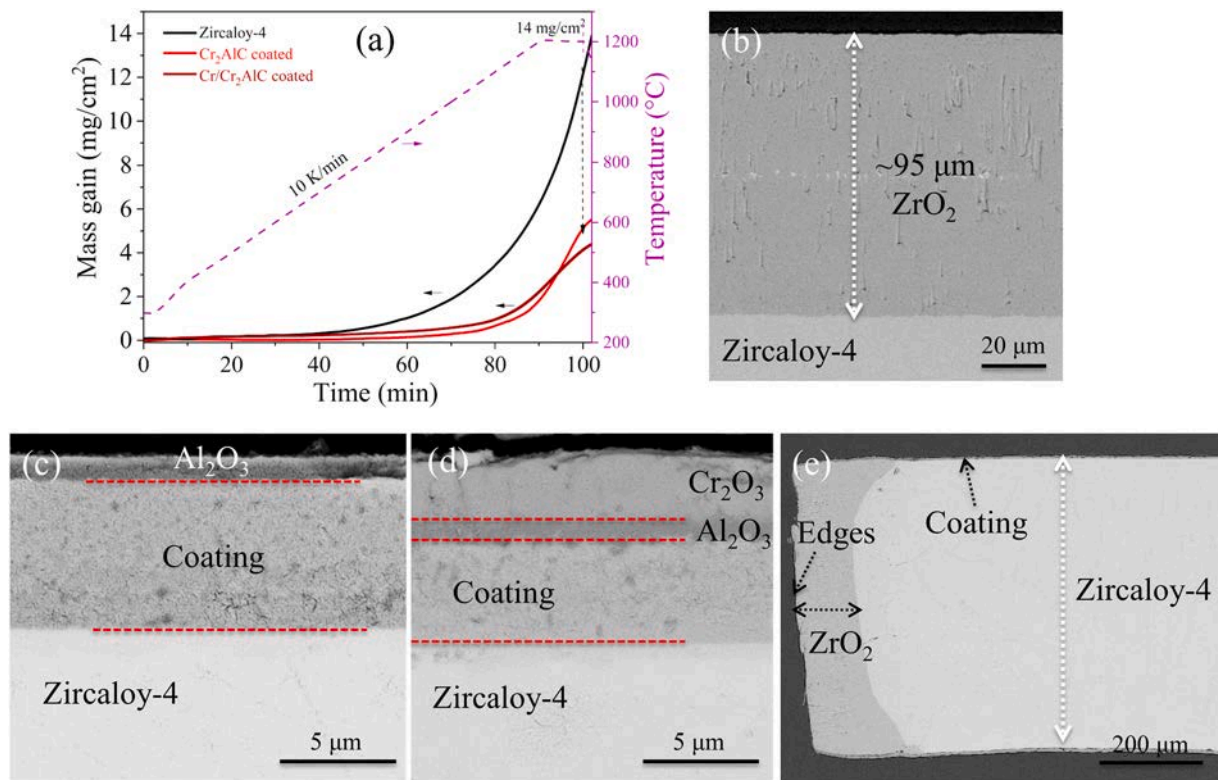
Fig. 11. Mass gain and oxide scale structure of uncoated and two coated Zircaloy-4 samples after transient tests from 300 °C to 1200 °C with 10 K/min heating rate and 10 min isothermal period at 1200 °C. (a) Mass gain curves during oxidation; cross-sectional SEM-BSE images (b) uncoated, (c) Type A-A (Cr_2AlC) coated, (d) and (e) Type B-A (Cr/Cr_2AlC) coated samples.

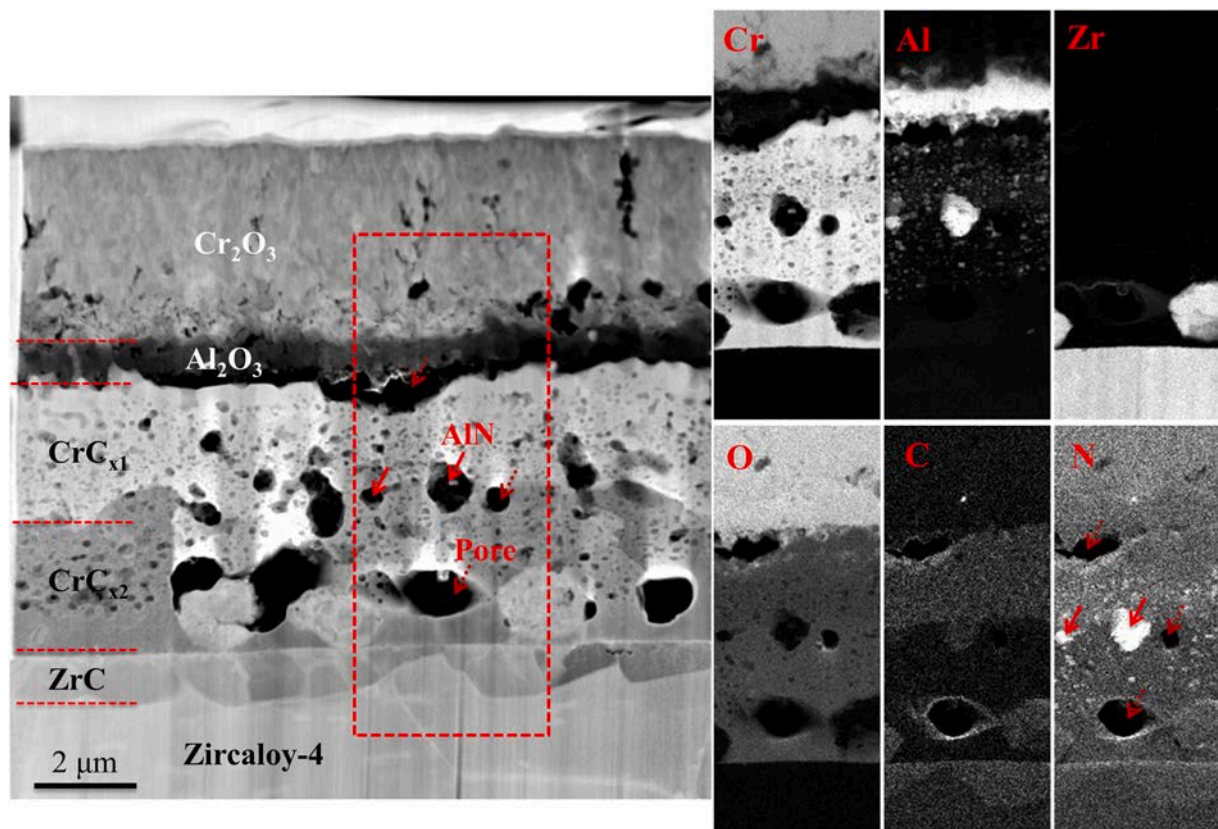**Fig. 12.** TEM images of the Type B-A (Cr/Cr_2AlC) coated Zircaloy-4 after transient test from 300 °C to 1200 °C in steam and corresponding EDS elemental mapping across the area marked by the red rectangle. The pores and AlN precipitates were marked by dashed and solid arrows, respectively.

mass gains during the tests, but clearly lower values compared to the uncoated sample, around 4 times lower after exposure (Fig. 11(a)). A thick ZrO_2 scale (nearly 100 μm) grew on the uncoated Zirclaoy-4, Fig. 11(b). Under identical conditions, a thin and dense α-Al_2O_3 scale or a bi-layered Cr_2O_3/α-Al_2O_3 scale formed on Type A-A (Cr_2AlC coated) and Type B-A (Cr/Cr_2AlC coated) samples, respectively, as shown in Fig. 11(c) and (d). The Cr_2O_3 sublayer (resulting from complete oxidation of the Cr overlayer) in Fig. 11 (d) was several times thicker than the α-Al_2O_3 layer. Obviously, the α-Al_2O_3 scale can provide better high-temperature oxidation resistance than the Cr_2O_3 scale with a slower growth rate. The uncoated edges were severely attacked by steam, and a thick ZrO_2 scale formed as displayed in Fig. 11(e) showing a cross-sectional image at low magnification. Steam penetrated profoundly into the interior regions at the corners. Thus, in the case of coated samples, the mass gains recorded in Fig. 11(a) were largely attributed to rapid oxidation of the uncoated edges, i.e. an edge effect occurred like before. The coatings exhibit good adherence without spallation, and only limited local failure of the coatings near the corners was observed. In all other regions, the coating protected the underneath Zircaloy-4 substrate from oxidation.

The coated samples were additionally characterized by TEM and results of the Cr/Cr_2AlC coated Zircaloy-4 are shown in Fig. 12 as an example. The bi-layered oxide scale was proven via EDS mapping. The Cr overlayer was completely oxidized and transformed into an exterior Cr_2O_3 layer. Selective oxidation of Al within the Cr_2AlC layer resulted in growth of an α-Al_2O_3 layer accompanied by a chromium carbide (CrC_x: Cr_7C_3 and Cr_3C_2) layer beneath. The two oxide sublayers (Cr_2O_3 and Al_2O_3) revealed good adhesion without delamination. Some pores existed at the α-Al_2O_3/CrC_x interface and within the CrC_x layer. In addition, partial delamination occurred at the α-Al_2O_3/CrC_x interface, which can be attributed to a weak interface and thermal stresses induced by temperature change during cooling [54]. Interestingly, the binary

chromium carbide layer separated into two sublayers (Fig. 12) with different carbon concentrations (lower in bottom layer) arising from inward diffusion of carbon into the substrate. The Cr bonding layer is not distinguishable in this image and a thin ZrC layer grew on the original Zircaloy-4 substrate surface.

Unlike isothermal oxidation at 1000 °C (Fig. 10), now no evident Al diffusion into the substrate and precipitation of some AlN particles were seen within the carbide layer. The main reasons for these dissimilar observations likely comprise higher oxidation temperature here increasing the outward diffusion flux of Al for external oxidation and AlN precipitates reducing the chemical activity of residual Al. The Al reservoir undoubtedly was rapidly depleted owing to the oxidation processes plus a thin Cr_2AlC coating layer. In addition, inward diffusion of C forming the ZrC layer may act as an unanticipated Al diffusion barrier. Formation of AlN precipitates can be explained by some residual air inside the furnace during oxidation, which has been frequently observed during oxidation of Al-containing alloys particularly in air atmosphere [55,56] In addition, Zr-enriched isolated particles were seen at the bottom of the carbide layer, presumably owing to rapid diffusion of Zr into the coatings along the columnar grain boundaries of the initial Cr bonding layer.

Transient tests from 500 °C to 1400 °C were conducted to explore the degradation/failure behavior of the coatings under severe conditions. The results including hydrogen release and oxide scale structure are presented in Fig. 13. The hydrogen concentration (or release) curve in Fig. 13(a) demonstrates a continuous and steady increase as a function of oxidation temperature with respect to uncoated Zircaloy-4. The hydrogen curves of the two coated samples overlapped together with lower values during the initial oxidation period. However, once the oxidation temperature reached specific high values an abrupt escalation phenomenon was seen.

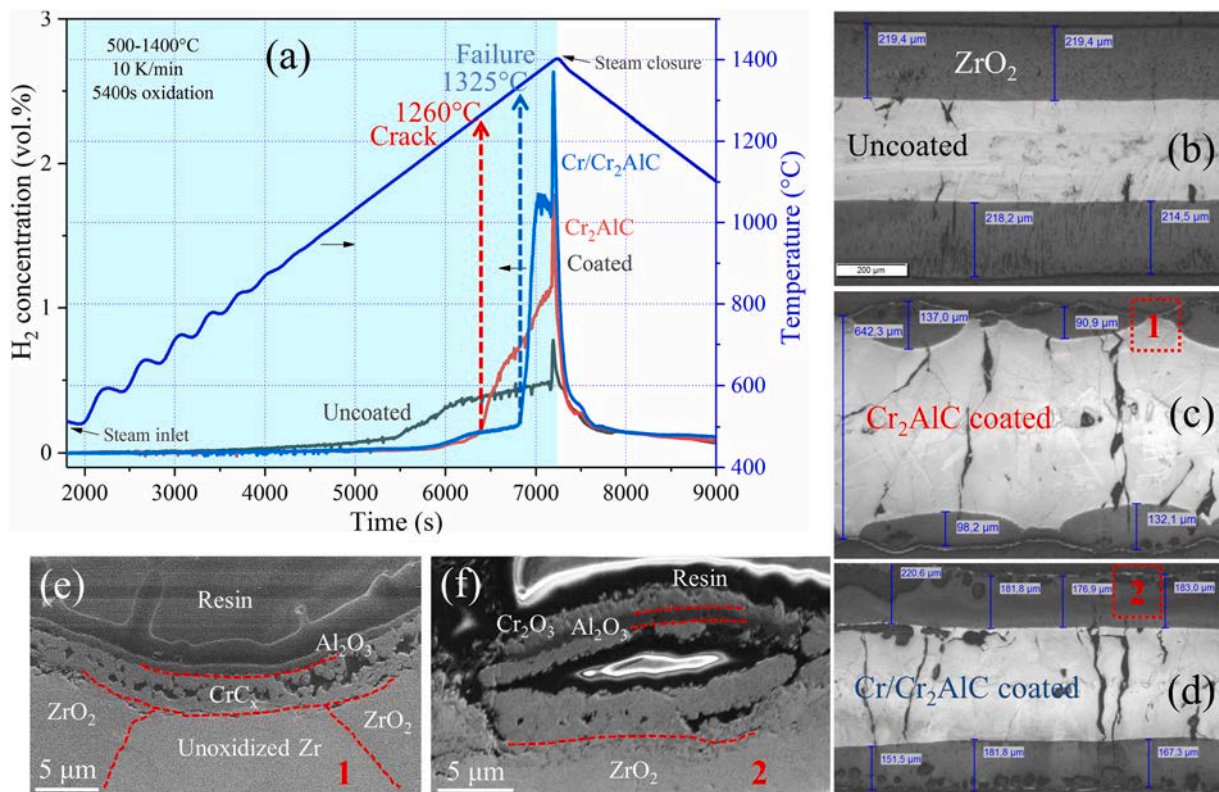The temperatures at which the curvature changes, marked by dashed

Fig. 13. Hydrogen release and oxide scale structure of uncoated and two coated Zircaloy-4 samples after transient tests from 500 °C to 1400 °C with 10 K/min heating rate. (a) Hydrogen release curves during oxidation, cross-sectional optical images (b) uncoated, (c) Type A-A (Cr_2AlC) coated, (d) Type B-A (Cr/Cr_2AlC) coated samples, SEM images (e) and (f) are taken at area 1 and 2, respectively.

arrows in Fig. 13(a), are ~1260 °C and 1325 °C for Cr$_2$AlC coated and Cr/Cr$_2$AlC coated samples, respectively. Both hydrogen release rates then surpassed the uncoated one at slightly higher temperatures. Apparently, both coatings lost their protective capability at such temperatures and rapid oxidation of the Zircaloy-4 substrates was initiated. The cross-sectional optical images evidence that uniform ZrO$_2$ layers formed on uncoated and Cr/Cr$_2$AlC coated samples, Fig. 13(b) and (d). In comparison, Cr$_2$AlC coated samples formed an uneven and discontinuous ZrO$_2$ layer, Fig. 13(c). In limited areas, the coating sustained its protective effect, and the Zircaloy-4 substrate was free of oxidation, Fig. 13(e). Thus, the hydrogen release behavior coupled with cross-sectional structures revealed that a single-layer Cr$_2$AlC coating underwent brittle fracture (macro-cracking) at ~1260 °C. The fracture is presumably connected with increasing stresses within the coating/substrate system induced by the oxidation process and mismatch in thermal expansion coefficients.

Via addition of a surface metallic layer (Cr overlayer), the Cr/Cr$_2$AlC coating evidently possesses higher ductility and fracture toughness. The loss of protective effect at ~1325 °C can be attributed to complete oxidation of the thin coatings. The reduced thickness of the Cr$_2$AlC layer (decreased to 75% of the original value) here obviously limits the reservoir of Al. Consequently, full oxidation of the Cr/Cr$_2$AlC coatings proceeds at a faster rate. The oxide scale configurations on both coatings, as displayed in Fig. 13(e) and (f), are similar as in previous oxidation tests.

3.3. Short-term hydrothermal corrosion

Short-term autoclave tests simulating typical PWR conditions to assess the hydrothermal corrosion performance of both coatings were conducted and the surface appearance and cross-sectional structure of the samples after testing are shown in Fig. 14.

Hydrothermal corrosion of uncoated Zircaloy-4 altered its original surface appearance from metallic luster to slightly gray. No noticeable transformation of color was seen before and after corrosion for the coated samples, Fig. 14(a). The uncoated Zircaloy-4 displayed a mass gain via formation of a thin and adherent ZrO$_2$ layer, Fig. 14(b). However, all four coated samples revealed mass loss with different levels of coating spallation. A lower level of spallation was seen on Cr/Cr$_2$AlC coated samples, as presented by the mass loss values. In addition, the majority of spallation occurred on the side that was not in contact with the sample holder during annealing. The discrepancy in cooling rates likely contributes to different residual stress states on the two sides after annealing, making one side more susceptible to cracking and spallation. Quantitative measurements of the residual stress using methods such as grazing-incidence X-ray diffraction [57] in the future will allow to gain a
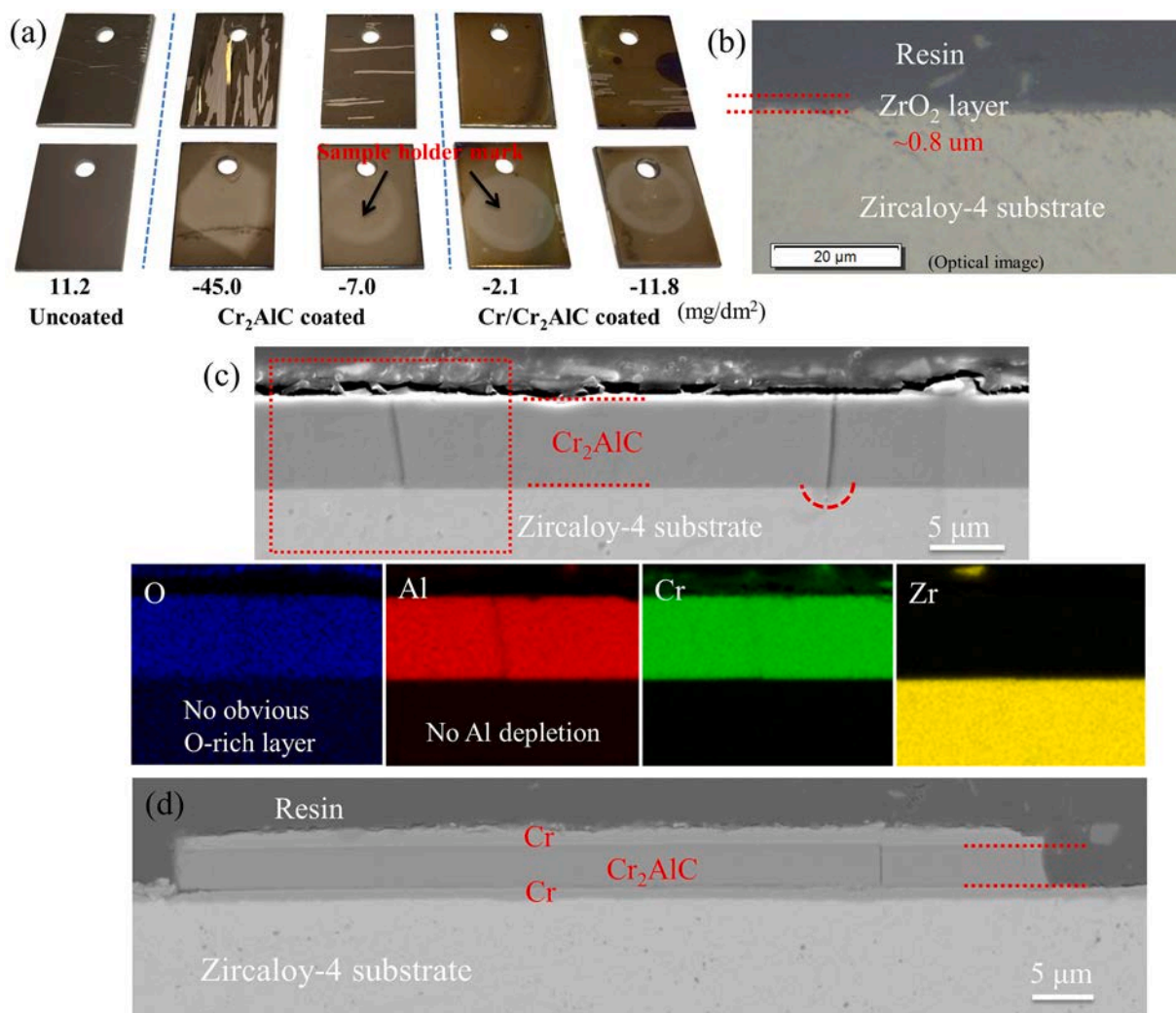

Fig. 14. Surface appearance and cross-sectional structure of uncoated and two coated Zircaloy-4 samples after 3 days autoclave test at 360 °C and 18.8 MPa. (a) Surface appearance, up row: first side, bottom row: second side, (b) uncoated Zirccaloy-4, (c) Type A-A (Cr$_2$AlC) coated with EDS elemental mapping in the area marked by red rectangle, (d) Type B-A (Cr/Cr$_2$AlC) coated sample.

more profound understanding of stress evolution and to adjust annealing conditions to avoid spallation.

As illustrated in Fig. 14(c), the Cr_2AlC coating revealed excellent hydrothermal corrosion resistance without detectable oxygen-rich layer and preferred dissolution of Al, even areas adjacent to the micro-cracks. The distribution of Al was homogeneous and did not show any signs of local depletion. The coating thickness remained unchanged. Only limited corrosion of the Zircaloy-4 substrate was observed underneath some cracks (marked by the semicircle). Recent longer-term autoclave testing (28 days at 300 °C and 12 MPa) of bulk MAX phases Ti_3SiC_2, Ti_3AlC_2, Ti_2AlC and Cr_2AlC indicated similar findings [47]. The Ti-based MAX phases cannot form a passivating oxide scale together with the preferential dissolution of the A-layer (Al or Si). However, there was virtually no change with respect to Cr_2AlC. The superior hydrothermal corrosion resistance of Cr_2AlC arises from its high Cr concentration permitting the formation of a passivating chromia scale, thereby impeding the rapid corrosion and preferential removal of Al. Long-term autoclave tests are required and planned to validate the hydrothermal corrosion performance of the coatings. The Cr/Cr_2AlC coating also possesses excellent corrosion resistance due to the presence of the Cr overlayer. Delamination of the coatings essentially occurred at the Cr_2AlC/Cr interface, as seen in Fig. 14(d), as a result of the mismatched thermal expansion coefficients between the Cr_2AlC and the Cr (as well as Zircaloy-4 substrate).

4. Discussion

4.1. Microstructure formation after annealing

Single-layer Cr_2AlC and bilayer Cr/Cr_2AlC coatings have been synthesized on Zircaloy-4 substrates in this study. The Cr_2AlC layers were realized via thermal annealing of Cr/C/Al nanoscale elemental multilayers deposited by magnetron sputtering, which were composed of basal-plane-oriented nano-crystallites and free of typical columnar growth. The specific microstructure formation for the Cr_2AlC layer is consistent with our previous studies on synthesizing Al-containing MAX phase carbides on SiO_2/Si and alumina substrate via the same method [41]. Annealing of Al/TiN multilayers to synthesize the Ti_2AlN MAX phase also resulted in a similar crystalline morphology before [58]. It is suggested that the multilayered architecture of the as-deposited precursors can adjust the growth model of the MAX phase during thermal annealing and allow unhindered growth of the grains in the lateral direction parallel to the multilayered interfaces [41]. In contrast, the Cr overlayer in the bilayer Cr/Cr_2AlC coatings which were deposited continuously from the Cr target shows a typical columnar grain structure, in line with the structural zone model (SZM) by Thornton [59]. In fact, the columnar structure also represents the most common grain morphology of PVD MAX phase coatings deposited directly from elemental targets or composite targets at high temperatures [23]. However, the platelet-like shaped grain structure without columnar grain boundaries of the Cr_2AlC coatings herein is favorable for oxidation and corrosion protection since the columnar grain boundaries often act as short-circuit diffusion path for oxidizing species [60].

Interfacial characterization between the Cr layer and Cr_2AlC layer within the annealed coatings by TEM indicated that no apparent diffusion or reaction occurs at the interface. The thermally-induced solid state diffusion reaction is largely constrained within the nanoscale multilayered stacks and the thick Cr layers (bonding layer and overlayer) are not involved under the selected annealing conditions. The nanoscale multilayers represent one type of energetic material with high chemical activity and stored chemical energy [61]. It can be anticipated that diffusion reaction is easily stimulated within the nanoscale multilayers initially to form MAX phase. The relatively low annealing temperature and short dwell time, i.e. 550 °C and 10 min, did not induce the observable interactions between the thick Cr layer and formed Cr_2AlC layer.

Both types of coatings display micro-cracking after annealing. The reasons can be associated with volume change during annealing and thermal expansion mismatch between the coating and substrate. The transformation of the Cr/C/Al nanoscale multilayers to Cr_2AlC MAX phase is associated with ~10% volume shrinkage, which will induce tensile stress within the coatings. The high mismatch in thermal expansion coefficients between the Cr_2AlC coating (11– 13.3×10^{-6} K^{-1}) and the Zircaloy-4 substrate (~$6 \times 10^{-6} K^{-1}$) can alter the residual stresses within the coatings from compression state before annealing to tensile state after annealing [33]. The thermal stress arising from temperature change and thermal expansion coefficients mismatch within the coating-substrate system can be estimated by following equation [62]:

$$\sigma_c = \frac{E_c (\alpha_s - \alpha_c)\Delta T}{(1 - \gamma_c) + (2t_cE_c/t_sE_s)(1 - \gamma_s)}$$

Here σ, E, α, ΔT, γ, and t symbolize thermal stress, Young's modulus, thermal expansion coefficient, temperature difference upon cooling, Poisson's ratio, and thickness, respectively. The subscripts c and s denote coating and substrate, respectively. To simplify, it is assumed that the coating only consists of a 6.5 μm thick Cr_2AlC layer. Based on previously reported values, E_c 250 GPa, E_s 575 GPa, α_c $13 \times 10^{-6} K^{-1}$, α_s 6×10^{-6} K^{-1}, γ_c 0.24, γ_s 0.37 are adopted [24]. The t_c 6.5 μm, t_s 575 μm and ΔT 550 K are applied. The calculated thermal stress (tensile) within the coating layer reaches ~1.2 GPa. This high value outweighs typical ultimate tensile and flexural strengths of ceramic materials including MAX phases [63]. Therefore, it can be anticipated that micro-cracking was triggered within the coating layer during the cooling period due to the aforementioned two aspects. However, it should be mentioned that the Zircaloy fuel cladding tubes are strongly textured with c-axis in hoop direction and their thermal expansion coefficient is anisotropic [64]. The differences in hoop and axial direction for cladding tubes may impose consequences on coating cracking. Coating deposition on cladding tubes is planned to address this issue.

4.2. Oxidation and hydrothermal corrosion performances

Selective oxidation of Al with preferential growth of Al_2O_3 scale on the single-layer Cr_2AlC coatings at high temperature in steam was confirmed in this study. A high chemical activity of Al in Cr_2AlC, attributing to its specific nanolaminated structure with weaker Cr—Al metallic bonding compared to stronger Cr—C covalent bonding, encourages the fast outward diffusion and selective oxidation of Al [54]. The potential forms (ions, atoms, or molecules) and transport nature of the steam-derived species in oxide scales during oxidation in steam atmosphere are not thoroughly understood and still of great debate [65,66]. But unlike oxidation in air, hydrogen (protons) or hydroxyl ions can be produced by dissociation of steam adsorbed on the oxide surface. Inward transport of hydroxyl ions across the oxide scale to the oxide/metal interface accompanied by released hydrogen outward diffusion is expected to occur. Since hydroxyl ions (OH^-) has a similar size that oxygen ions (O^{2-}), and protons (H^+) are much smaller than above two ions. The oxidation rate can be slightly enhanced and the alumina scale adherence could also be reduced in steam (due to formation of hydroxides at interface [65]) than oxidation in air. Compared with previous intensive investigations of Cr_2AlC bulk or coating oxidized in air [26,29,45,46,67], the pure steam atmosphere does not evidently degrade its oxidation performance and alumina scale grows on both air and steam atmospheres.

Oxide scale formed on the bilayer Cr/Cr_2AlC coatings reveals a much lower growth rate of alumina scale compared to chromia scale and detrimental effect of columnar grain boundaries to the oxidation resistance. The columnar grain boundaries of Cr overlayer act as rapid diffusion paths for oxidizing species, leading to internal oxidation of the beneath Cr_2AlC layer. Similar internal oxidation behavior of Zr alloy substrates has been reported before for other columnar coatings [60].

While in our case the growth of thin alumina layer at Cr/Cr$_2$AlC interface owing to internal oxidation can stop further inward diffusion of oxidizing species into the alloy substrate before failure of the coatings. Otherwise, the internal oxidation of the Zr alloy substrates will make the fuel cladding hard and brittle.

Oxidation degradation of both types of coatings mainly connects with Al depletion and void/pore formation [26,33]. The Al depletion occurs via two different diffusion processes during oxidation: outward diffusion to form alumina scale and inward diffusion to the alloy substrate (interdiffusion between coating and substrate). It is necessary to mention that the inward diffusion of Al was found to be greatly suppressed during oxidation at 1200 °C compared to at 1000 °C. The inward diffusion of carbon then became the dominant process. As explained before, the main reason can be attributed to remarkably enhanced outward diffusion flux of Al for external oxidation with increasing temperature and limited Al reservoir of thin coatings. Depletion of Al results in dissociation of the Cr$_2$AlC layer into binary Cr—C carbides and void nucleation/growth. After the complete consumption of the Al, oxidation of the binary chromium carbides will continue with formation of Cr$_2$O$_3$ and gaseous carbon oxides, which will increase the density of voids within the coatings. The coatings thus will finally lose its protective effect either by macro-cracking or complete oxidation, as seen in the transient tests. The failure temperatures for the single-layer Cr$_2$AlC and bilayer Cr/Cr$_2$AlC coatings are ~1260 °C and 1325 °C, respectively, as identified by hydrogen production in the transient test up to 1400 °C. Their failure temperatures are slightly lower than the accepted maximum protective temperature for pure Cr coatings, i.e. Cr—Zr eutectic temperature (~1330 °C). However, it should be mentioned that the Cr$_2$AlC-based coatings here are much thinner than typical Cr coatings deposited for ATF application. Increasing the coating thickness is foreseen to enhance its protective capability to higher temperatures in steam.

Both single-layer Cr$_2$AlC and bilayer Cr/Cr$_2$AlC coatings display excellent hydrothermal corrosion resistance with formation of a passivating chromia scale on the surface. The excellent hydrothermal corrosion resistance of Cr coatings in simulated PWR normal conditions has been validated by long-term autoclave tests [68]. The autoclave tests of Cr$_2$AlC coatings in this study and Cr$_2$AlC bulk reported previously [47] reveal that the high Cr concentration also allows Cr$_2$AlC to form a passivating chromia scale under hydrothermal corrosion conditions. A combination of excellent oxidation resistance (protective Al$_2$O$_3$ scale formation) and hydrothermal corrosion resistance (passivating Cr$_2$O$_3$ scale formation) implies its great potential for ATF application.

One common challenge for utilization of ceramic coatings for ATF application is their relatively low fracture toughness, which makes them susceptible to cracking and spallation when suffering high stresses or cyclic stresses [7]. Micro-cracking and partial spallation were also seen for the Cr$_2$AlC-based coatings during oxidation and corrosion tests in this study. While, the bilayer Cr/Cr$_2$AlC coatings have shown better mechanical properties compared to the single-layer Cr$_2$AlC coatings, as proved by the higher failure temperature in transient oxidation test and less level of spallation after autoclave test. Multilayered coatings consisting of both metallic and ceramic sublayers have been frequently designed to overcome the weakness of single-layer coatings with improved mechanical and corrosion properties [69,70]. Via adjusting the modulation ratio between Cr and Cr$_2$AlC layer, Cr/Cr$_2$AlC multilayered coatings could achieve both good mechanical properties and oxidation/corrosion resistance.

5. Conclusions

Single-layer Cr$_2$AlC and bilayer Cr/Cr$_2$AlC coatings were synthesized on Zircaloy-4 substrates via thermal annealing of magnetron-sputtered nanoscale elemental multilayers at 550 °C for 10 min. Their high-temperature oxidation performance in steam and short-term hydrothermal corrosion behavior in an autoclave were studied to evaluate

their application capability as coated ATF claddings. The main conclusions are summarized below:

(1) The as-deposited nanoscale elemental multilayers transform to single-phase and basal-plane textured Cr$_2$AlC MAX phase via thermally-induced solid state diffusion reaction. The annealed coatings showed parallel micro-cracks on the surface due to thermal expansion coefficients mismatch between the Cr$_2$AlC and Zircaloy-4 and volume change during diffusion reaction.

(2) Oxidation of single-layer Cr$_2$AlC coatings in high-temperature steam resulted in growth of a dense and adherent α-Al$_2$O$_3$ scale. A bi-layered oxide scale structure, i.e. Cr$_2$O$_3$/α-Al$_2$O$_3$, formed on Cr/Cr$_2$AlC coatings. Oxidation and inward diffusion induced depletion of Al caused transformation of the Cr$_2$AlC layer to a porous layer consisting of CrC$_x$ and un-oxidized Cr$_2$AlC initially. Micro-cracks on both coatings can be self-healed after oxidation at 1000 °C for 1 h via growth of alumina associated with corresponding volume expansion.

(3) Transient tests up to 1400 °C in steam revealed that single-layer Cr$_2$AlC and bilayer Cr/Cr$_2$AlC coatings lost their protective effect via macro-cracking and complete oxidation, respectively. The bilayer Cr/Cr$_2$AlC coatings possessed better mechanical properties and failed at a higher temperature compared to single-layer Cr$_2$AlC coatings.

(4) Autoclave tests simulating typical PWR conditions for 3 days discovered that both coatings, Cr$_2$AlC and Cr/Cr$_2$AlC, displayed excellent hydrothermal corrosion resistance without detectable oxygen-rich layer and preferred dissolution of Al.

To enhance the coating performance avoiding premature failure, micro-cracking of the annealed coatings has to be avoided, for instance by introducing a suitable interlayer or adjusting annealing process. Long-term autoclave tests are still required to validate their hydrothermal corrosion performance. In addition, the oxidation performance and degradation modes of the coatings after substantial time of hydrothermal corrosion in nominal conditions are needed to better simulate actual accidental scenarios. Multilayered designs with numerous sublayers to improve the mechanical properties of the Cr$_2$AlC-based coatings are of interest for future studies.

CRediT authorship contribution statement

Chongchong Tang: Conceptualization, Methodology, Investigation, Writing – original draft, Writing – review & editing, Project administration. **Mirco Große:** Investigation, Writing – review & editing. **Sven Ulrich:** Resources, Writing – review & editing. **Michael Klimenkov:** Investigation, Writing – review & editing. **Ute Jantsch:** Investigation, Writing – review & editing. **Hans Jürgen Seifert:** Resources, Writing – review & editing. **Michael Stüber:** Conceptualization, Resources, Writing – review & editing. **Martin Steinbrück:** Investigation, Resources, Writing – review & editing.

Declaration of competing interest

The authors declare that they have no known competing financial interests or personal relationships that could have appeared to influence the work reported in this paper.

References

[1] M. Schütze, W.J. Quadakkers, Future directions in the field of high-temperature corrosion research, Oxid, Met. 87 (2017) 681–704, https://doi.org/10.1007/s11085-017-9719-3.

[2] N.P. Padture, M. Gell, E.H. Jordan, Thermal barrier coatings for gas-turbine engine applications, Science (80-.) 296 (2002) 280–284.

[3] M. Steinbrück, M. Große, L. Sepold, J. Stuckert, Synopsis and outcome of the QUENCH experimental program, Nucl, Eng. Des. 240 (2010) 1714–1727, https://doi.org/10.1016/j.nucengdes.2010.03.021.

[4] S.J. Zinkle, K.A. Terrani, J.C. Gehin, L.J. Ott, L.L. Snead, Accident tolerant fuels for LWRs: a perspective, J. Nucl. Mater. 448 (2014) 374–379, https://doi.org/10.1016/j.jnucmat.2013.12.005.

[5] Z. Duan, H. Yang, Y. Satoh, K. Murakami, S. Kano, Z. Zhao, J. Shen, H. Abe, Current status of materials development of nuclear fuel cladding tubes for light water reactors, Nucl, Eng. Des. 316 (2017) 131–150, https://doi.org/10.1016/j.nucengdes.2017.02.031.

[6] K.A. Terrani, Accident tolerant fuel cladding development: promise, status, and challenges, J. Nucl. Mater. 501 (2018) 13–30, https://doi.org/10.1016/j.jnucmat.2017.12.043.

[7] C. Tang, M. Stueber, H.J. Seifert, M. Steinbrueck, Protective coatings on zirconium-based alloys as accident-tolerant fuel (ATF) claddings, Corros, Rev. 35 (2017) 141–166, https://doi.org/10.1515/corrrev-2017-0010.

[8] H.-G. Kim, I.-H. Kim, Y.-I. Jung, D.-J. Park, J.-Y. Park, Y.-H. Koo, Adhesion property and high-temperature oxidation behavior of Cr-coated Zircaloy-4 cladding tube prepared by 3D laser coating, J. Nucl. Mater. 465 (2015) 531–539, https://doi.org/10.1016/j.jnucmat.2015.06.030.

[9] H. Yeom, B. Maier, G. Johnson, T. Dabney, M. Lenling, K. Sridharan, High temperature oxidation and microstructural evolution of cold spray chromium coatings on Zircaloy-4 in steam environments, J. Nucl. Mater. 526 (2019), 151737, https://doi.org/10.1016/j.jnucmat.2019.151737.

[10] X. Han, J. Xue, S. Peng, H. Zhang, An interesting oxidation phenomenon of Cr coatings on Zry-4 substrates in high temperature steam environment, Corros, Sci. 156 (2019) 117–124, https://doi.org/10.1016/j.corsci.2019.05.017.

[11] J.-C. Brachet, I. Idarraga-Trujillo, M. Le Flem, M. Le Saux, V. Vandenberghe, S. Urvoy, E. Rouesne, T. Guilbert, C. Toffolon-Masclet, M. Tupin, C. Phalippou, F. Lomello, F. Schuster, A. Billard, G. Velisa, C. Ducros, F. Sanchette, Early studies on Cr-coated Zircaloy-4 as enhanced accident tolerant nuclear fuel claddings for light water reactors, J. Nucl. Mater. 517 (2019) 268–285, https://doi.org/10.1016/j.jnucmat.2019.02.018.

[12] T. Wei, R. Zhang, H. Yang, H. Liu, S. Qiu, Y. Wang, P. Du, K. He, X. Hu, C. Dong, Microstructure, corrosion resistance and oxidation behavior of Cr-coatings on Zircaloy-4 prepared by vacuum arc plasma deposition, Corros, Sci. 158 (2019), 108077, https://doi.org/10.1016/j.corsci.2019.06.029.

[13] A.S. Kuprin, V.A. Belous, V.N. Voyevodin, R.L. Vasilenko, V.D. Ovcharenko, G. D. Tolstolutskaya, I.E. Kopanets, I.V. Kolodiy, Irradiation resistance of vacuum arc chromium coatings for zirconium alloy fuel claddings, J. Nucl. Mater. 510 (2018) 163–167, https://doi.org/10.1016/j.jnucmat.2018.07.063.

[14] M. Ševeček, A. Gurgen, A. Seshadri, Y. Che, M. Wagih, B. Phillips, V. Champagne, K. Shirvan, Development of Cr cold spray–coated fuel cladding with enhanced accident tolerance, Nucl, Eng. Technol. 50 (2018) 229–236, https://doi.org/10.1016/j.net.2017.12.011.

[15] K. Hong, J.R. Barber, M.D. Thouless, W. Lu, Cracking of Cr-coated accident-tolerant fuel during normal operation and under power-ramping conditions, Nucl, Eng. Des. 353 (2019) 110275, https://doi.org/10.1016/j.nucengdes.2019.110275.

[16] A. Wu, J. Ribis, J.C. Brachet, E. Clouet, F. Leprêtre, E. Bordas, B. Arnal, HRTEM and chemical study of an ion-irradiated chromium/zircaloy-4 interface, J. Nucl. Mater. 504 (2018) 289–299, https://doi.org/10.1016/j.jnucmat.2018.01.029.

[17] J.C. Brachet, E. Rouesne, J. Ribis, T. Guilbert, S. Urvoy, G. Nony, C. Toffolon-Masclet, M. Le Saux, N. Chaabane, H. Palancher, A. David, J. Bischoff, J. Augereau, E. Pouillier, High temperature steam oxidation of chromium-coated zirconium-based alloys: kinetics and process, Corros, Sci. 167 (2020), https://doi.org/10.1016/j.corsci.2020.108537.

[18] A.S. Dorcheh, M. Schütze, M.C. Galetz, Factors affecting isothermal oxidation of pure chromium in air, Corros, Sci. 130 (2018) 261–269, https://doi.org/10.1016/j.corsci.2017.11.006.

[19] E.J. Opila, N.S. Jacobson, D.L. Myers, E.H. Copland, Predicting oxide stability in high-temperatue water vapor, JOM, 58 (2006) 22–28.

[20] B. Maier, H. Yeom, G. Johnson, T. Dabney, J. Walters, J. Romero, H. Shah, P. Xu, K. Sridharan, Development of cold spray coatings for accident-tolerant fuel cladding in light water reactors, Jom 70 (2018) 198–202, https://doi.org/10.1007/s11837-017-2643-9.

[21] C. Tang, M. Grosse, Martin Steinbrueck, K. Shirvan, Oxidation and quench behavior of cold spraying Cr-coated zircaloy fuel cladding under severe accident scenarios, in: TopFuel 2019, 2019, pp. 855–863.

[22] M.W. Barsoum, The MN+1AXN phases: a new class of solids; thermodynamically stable nanolaminates, Prog, Sol. State Chem. 28 (2000) 201–281, https://doi.org/10.1016/S0079-6786(00)00006-6.

[23] P. Eklund, M. Beckers, U. Jansson, H. Hogberg, L. Hultman, The Mn+1AXn phases: materials science and thin-film processing, Thin Solid Films 518 (2010) 1851–1878, https://doi.org/10.1016/j.tsf.2009.07.184.

[24] Z. Lin, Y. Zhou, M. Li, Synthesis, microstructure, and property of Cr2AlC, J. Mater. Sci. Technol. 23 (2007) 721–746.

[25] W. Tian, P. Wang, G. Zhang, Y. Kan, Y. Li, D. Yan, Synthesis and thermal and electrical properties of bulk Cr2AlC, Scr. Mater. 54 (2006) 841–846, https://doi.org/10.1016/j.scriptamat.2005.11.009.

[26] D.E. Hajas, M. to Baben, B. Hallstedt, R. Iskandar, J. Mayer, J.M. Schneider, Oxidation of Cr2AlC coatings in the temperature range of 1230 to 1410°C, Surf. Coat. Technol. 206 (2011) 591–598, https://doi.org/10.1016/j.surfcoat.2011.03.086.

[27] D.J. Tallman, B. Anasori, M.W. Barsoum, A critical review of the oxidation of Ti2AlC, Ti3AlC2 and Cr2AlC in air, Mater, Res. Lett. 1 (2013) 115–125, https://doi.org/10.1080/21663831.2013.806364.

[28] R. Pei, S.A. McDonald, L. Shen, S. van der Zwaag, W.G. Sloof, P.J. Withers, P. M. Mummery, Crack healing behaviour of Cr2AlC MAX phase studied by X-ray tomography, J. Eur. Ceram. Soc. 37 (2017) 441–450, https://doi.org/10.1016/j.jeurceramsoc.2016.07.018.

[29] O. Berger, R. Boucher, M. Ruhnow, Part II. Oxidation of yttrium doped Cr2AlC films in temperature range between 700 and 1200° C, Surf, Eng. 31 (2015) 386–396, https://doi.org/10.1179/1743294414Y.0000000418.

[30] B.R. Maier, B.L. Garcia-Diaz, B. Hauch, L.C. Olson, R.L. Sindelar, K. Sridharan, Cold spray deposition of Ti2AlC coatings for improved nuclear fuel cladding, J. Nucl. Mater. 466 (2015) 712–717, https://doi.org/10.1016/j.jnucmat.2015.06.028.

[31] J.G. Gigax, M. Kennas, H. Kim, T. Wang, B.R. Maier, H. Yeom, G.O. Johnson, K. Sridharan, L. Shao, Radiation response of Ti2AlC MAX phase coated Zircaloy-4 for accident tolerant fuel cladding, J. Nucl. Mater. 523 (2019) 26–32, https://doi.org/10.1016/j.jnucmat.2019.05.021.

[32] W. Li, Z. Wang, J. Shuai, B. Xu, A. Wang, P. Ke, A high oxidation resistance Ti2AlC coating on Zirlo substrates for loss-of-coolant accident conditions, Ceram. Int. 45 (2019) 13912–13922, https://doi.org/10.1016/j.ceramint.2019.04.089.

[33] M. Ougier, A. Michau, F. Lomello, F. Schuster, H. Maskrot, M.L. Schlegel, High-temperature oxidation behavior of HiPIMS as-deposited Cr–Al–C and annealed Cr2AlC coatings on Zr-based alloy, J. Nucl. Mater. 528 (2020), 151855, https://doi.org/10.1016/j.jnucmat.2019.151855.

[34] Q.M. Wang, A. Flores Renteria, O. Schroeter, R. Mykhaylonka, C. Leyens, W. Garkas, M. to Baben, Fabrication and oxidation behavior of Cr2AlC coating on Ti6242 alloy, Surf. Coat. Technol. 204 (2010) 2343–2352, https://doi.org/10.1016/j.surfcoat.2010.01.002.

[35] J.L. Smialek, J.A. Nesbitt, T.P. Gabb, A. Garg, R.A. Miller, Hot corrosion and low cycle fatigue of a Cr2AlC-coated superalloy, Mater. Sci. Eng. A 711 (2018) 119–129, https://doi.org/10.1016/j.msea.2017.10.098.

[36] F. Fejt, M. Sevecek, J. Frybort, O. Novak, Study on neutronics of VVER-1200 with accident tolerant fuel cladding, Ann. Nucl. Energy 124 (2019) 579–591, https://doi.org/10.1016/j.anucene.2018.10.040.

[37] M. Sonestedt, J. Frodelius, M. Sundberg, L. Hultman, K. Stiller, Oxidation of Ti2AlC bulk and spray deposited coatings, Corros, Sci. 52 (2010) 3955–3961, https://doi.org/10.1016/j.corsci.2010.08.004.

[38] C. Tang, M. Steinbrueck, M. Stueber, M. Grosse, X. Yu, S. Ulrich, H.J. Seifert, Deposition, characterization and high-temperature steam oxidation behavior of single-phase Ti2AlC-coated Zircaloy-4, Corros, Sci. 135 (2018) 87–98, https://doi.org/10.1016/j.corsci.2018.02.035.

[39] J.J. Li, L.F. Hu, F.Z. Li, M.S. Li, Y.C. Zhou, Variation of microstructure and composition of the Cr2AlC coating prepared by sputtering at 370 and 500 °C, Surf. Coat. Technol. 204 (2010) 3838–3845, https://doi.org/10.1016/j.surfcoat.2010.04.067.

[40] R. Grieseler, B. Hahnlein, M. Stubenrauch, T. Kups, M. Wilke, M. Hopfeld, J. Pezoldt, P. Schaaf, Nanostructured plasma etched, magnetron sputtered nanolaminar Cr2AlC MAX phase thin films, Appl. Surf. Sci. 292 (2014) 997–1001, https://doi.org/10.1016/j.apsusc.2013.12.099.

[41] C. Tang, M. Steinbrück, M. Klimenkov, U. Jantsch, H.J. Seifert, S. Ulrich, M. Stüber, Textured growth of polycrystalline MAX phase carbide coatings via thermal annealing of M/C/Al multilayers, J. Vac. Sci. Technol. A. 38 (2020), 013401, https://doi.org/10.1116/1.5131544.

[42] J. Zhang, Z. Tian, H. Zhang, L. Zhang, J. Wang, On the chemical compatibility between Zr-4 substrate and well-bonded Cr2AlC coating, J. Mater. Sci. Technol. 35 (2019) 1–5, https://doi.org/10.1016/j.jmst.2018.09.005.

[43] S. Mráz, M. Tyra, M. to Baben, M. Hans, X. Chen, F. Herrig, K. Lambrinou, J. M. Schneider, Thermal stability enhancement of Cr2AlC coatings on Zr by utilizing a double layer diffusion barrier, J. Eur. Ceram. Soc. 40 (2019) 1119–1124, https://doi.org/10.1016/j.jeurceramsoc.2019.10.008.

[44] C. Tang, M.K. Grosse, P. Trtik, M. Steinbrück, M. Stüber, H.J. Seifert, H2 permeation behavior of Cr2AlC and Ti2AlC MAX phase coated Zircaloy-4 by neutron radiography, Acta Polytech. 58 (2018) 69–76, https://doi.org/10.14311/AP.2018.58.0069.

[45] J.J. Li, M.S. Li, H.M. Xiang, X.P. Lu, Y.C. Zhou, Short-term oxidation resistance and degradation of Cr2AlC coating on M38G superalloy at 900-1100 °C, Corros, Sci. 53 (2011) 3813–3820, https://doi.org/10.1016/j.corsci.2011.07.032.

[46] Q.M. Wang, R. Mykhaylonka, A. Flores Renteria, J.L. Zhang, C. Leyens, K.H. Kim, Improving the high-temperature oxidation resistance of a β-γ TiAl alloy by a Cr2AlC coating, Corros, Sci. 52 (2010) 3793–3802, https://doi.org/10.1016/j.corsci.2010.07.031.

[47] J. Ward, D. Bowden, E. Prestat, S. Holdsworth, D. Stewart, M.W. Barsoum, M. Preuss, P. Frankel, Corrosion performance of Ti3SiC2, Ti3AlC2, Ti2AlC and Cr2AlC MAX phases in simulated primary water conditions, Corros, Sci. 139 (2018) 444–453, https://doi.org/10.1016/j.corsci.2018.04.034.

[48] Y. Du, J.-X. Liu, J. Gu, X.-G. Wang, F. Xu, G.-J. Zhang, Anisotropic corrosion of Ti2AlC and Ti3AlC2 in supercritical water at 500 oC, Ceram. Int. 43 (2017) 7166–7171, https://doi.org/10.1016/j.ceramint.2017.02.153.

[49] E. Alat, A.T. Motta, R.J. Comstock, J.M. Partezana, D.E. Wolfe, Multilayer (TiN, TiAlN) ceramic coatings for nuclear fuel cladding, J. Nucl. Mater. 478 (2016) 236–244, https://doi.org/10.1016/j.jnucmat.2016.05.021.

[50] M. Steinbrück, Oxidation of boron carbide at high temperatures, J. Nucl. Mater. 336 (2005) 185–193, https://doi.org/10.1016/j.jnucmat.2004.09.022.

[51] P.H. Mayrhofer, C. Mitterer, L. Hultman, H. Clemens, Microstructural design of hard coatings, Prog, Mater. Sci. 51 (2006) 1032–1114, https://doi.org/10.1016/j.pmatsci.2006.02.002.

[52] A. Paul, M.J.H. Van Dal, A.A. Kodentsov, F.J.J. Van Loo, The Kirkendall effect in multiphase diffusion, Acta Mater. 52 (2004) 623–630, https://doi.org/10.1016/j.actamat.2003.10.007.

[53] M. Steinbrück, N. Vér, M. Große, Oxidation of advanced zirconium cladding alloys in steam at temperatures in the range of 600-1200 °C, Oxid, Met. 76 (2011) 215–232, https://doi.org/10.1007/s11085-011-9249-3.

[54] D.B. Lee, T.D. Nguyen, Cyclic oxidation of Cr2AlC between 1000 and 1300°C in air, J. Alloys Compd. 464 (2008) 434–439, https://doi.org/10.1016/j.jallcom.2007.10.018.

[55] T.M. Butler, J.P. Alfano, R.L. Martens, M.L. Weaver, High-temperature oxidation behavior of Al-co-Cr-Ni-(Fe or Si) multicomponent high-entropy alloys, Jom. 67 (2015) 246–259, https://doi.org/10.1007/s11837-014-1185-7.

[56] U. Krupp, H.J. Christ, Selective oxidation and internal nitridation during high-temperature exposure of single-crystalline nickel-base superalloys, Metall. Mater. Trans. A Phys. Metall. Mater. Sci. 31 (2000) 47–56, https://doi.org/10.1007/s11661-000-0051-0.

[57] C. Ma, J. Huang, H. Chen, Residual stress measurement in textured thin film by grazing-incidence X-ray diffraction, Thin Solid Films 418 (2002) 73–78, https://doi.org/10.1016/S0040-6090(02)00680-6.

[58] L. Groner, L. Kirste, S. Oeser, A. Fromm, M. Wirth, F. Meyer, F. Burmeister, C. Eberl, Microstructural investigations of polycrystalline Ti2AlN prepared by physical vapor deposition of Ti-AlN multilayers, Surf. Coat. Technol. 343 (2018) 166–171, https://doi.org/10.1016/j.surfcoat.2017.09.042.

[59] J.A. Thornton, High rate thick film growth, Annu. Rev. Mater. Sci. 7 (1977) 239–260, https://doi.org/10.1146/annurev.ms.07.080177.001323.

[60] Y. Dong, H. Zhu, F. Ge, G. Zhao, F. Huang, Microstructural effects on the high-temperature steam oxidation resistance of magnetron sputtered Cr-Al-Si-N quaternary coatings on zirconium coupons, Surf. Coat. Technol. 374 (2019) 393–401, https://doi.org/10.1016/j.surfcoat.2019.06.013.

[61] D.P. Adams, Reactive multilayers fabricated by vapor deposition: a critical review, Thin Solid Films 576 (2015) 98–128, https://doi.org/10.1016/j.tsf.2014.09.042.

[62] V. Teixeira, Residual stress and cracking in thin PVD coatings, Vacuum. 64 (2002) 393–399, https://doi.org/10.1016/S0042-207X(01)00327-X.

[63] M.W. Barsoum, M. Radovic, Elastic and mechanical properties of the MAX phases, Annu. Rev. Mater. Res. 41 (2011) 195–227, https://doi.org/10.1146/annurev-matsci-062910-100448.

[64] K.L. Murty, I. Charit, Texture development and anisotropic deformation of zircaloys, Prog. Nucl. Energy 48 (2006) 325–359, https://doi.org/10.1016/j.pnucene.2005.09.011.

[65] S.R.J. Saunders, M. Monteiro, F. Rizzo, The oxidation behaviour of metals and alloys at high temperatures in atmospheres containing water vapour: a review, Prog, Mater. Sci. 53 (2008) 775–837, https://doi.org/10.1016/j.pmatsci.2007.11.001.

[66] I.G. Wright, R.B. Dooley, A review of the oxidation behaviour of structural alloys in steam, Int. Mater. Rev. 55 (2010) 129–167, https://doi.org/10.1179/095066010X12646898728165.

[67] D.B. Lee, T.D. Nguyen, J.H. Han, S.W. Park, Oxidation of Cr2AlC at 1300°C in air, Corros, Sci. 49 (2007) 3926–3934, https://doi.org/10.1016/j.corsci.2007.03.044.

[68] J. Bischoff, C. Delafoy, C. Vauglin, P. Barberis, C. Roubeyrie, D. Perche, D. Duthoo, F. Schuster, J.C. Brachet, E.W. Schweitzer, K. Nimishakavi, AREVA NP's enhanced accident-tolerant fuel developments: focus on Cr-coated M5 cladding, Nucl, Eng. Technol. 50 (2018) 223–228, https://doi.org/10.1016/j.net.2017.12.004.

[69] P. Wieciński, J. Smolik, H. Garbacz, K.J. Kurzydłowski, Failure and deformation mechanisms during indentation in nanostructured Cr/CrN multilayer coatings, Surf. Coat. Technol. 240 (2014) 23–31, https://doi.org/10.1016/j.surfcoat.2013.12.006.

[70] S. PalDey, S.C. Deevi, Single layer and multilayer wear resistant coatings of (Ti,Al)N: a review, Mater. Sci. Eng. A 342 (2003) 58–79, https://doi.org/10.1016/S0921-5093(02)00259-9.

Repository KITopen

Dies ist ein Postprint/begutachtetes Manuskript.